

This document is the Accepted Manuscript version of a Published Work that appeared in final form in ACS Nano, copyright © American Chemical Society after peer review and technical editing by the publisher.

To access the final edited and published work see  
<https://pubs.acs.org/articlesonrequest/AOR-tbnWYnqwwCzq9eMnfStF>.

# Zig-Zag $sp^2$ Carbon Chains Passing through $sp^3$

## Framework – A Driving Force toward Room

## Temperature Ferromagnetic Graphene

*Jiří Tuček,<sup>†</sup> Kateřina Holá,<sup>†</sup> Giorgio Zoppellaro,<sup>†</sup> Piotr Błoński,<sup>†</sup> Rostislav Langer,<sup>†</sup> Miroslav Medved',<sup>†</sup> Toma Susi,<sup>‡</sup> Michal Otyepka,<sup>†,\*</sup> and Radek Zbořil<sup>†,\*</sup>*

<sup>†</sup> Regional Centre of Advanced Technologies and Materials, Department of Physical Chemistry, Faculty of Science, Palacký University in Olomouc, Šlechtitelů 27, 783 71 Olomouc, Czech Republic.

<sup>‡</sup> University of Vienna, Faculty of Physics, Boltzmannngasse 5, 1090 Vienna, Austria.

ABSTRACT: Stabilization of ferromagnetic ordering in graphene-based systems up to room temperature remains an important challenge owing to huge scope for applications in electronics, spintronics, biomedicine, and separation technologies. To date, several strategies have been proposed, including edge engineering, introduction of defects and dopants, and covalent functionalization. However, these techniques are usually hampered by limited temperature sustainability of ferromagnetic ordering. Here, we describe a method for the well-controlled  $sp^2$  functionalization of graphene to synthesize zig-zag conjugated  $sp^2$  carbon chains that can act as communication pathways among radical motifs. Zig-zag  $sp^2/sp^3$  patterns in the basal plane were clearly observed by high-resolution scanning transmission electron microscopy and provided a suitable matrix for stabilization of ferromagnetic ordering up to room temperature due to combined contributions of itinerant  $\pi$ -electrons and superexchange interactions. The results highlight the principal role of  $sp^2/sp^3$  ratio and super-organization of radical motifs in graphene for generating room temperature non-metallic magnets.

KEYWORDS: hydroxofluorographene • fluorographene • magnetic carbon • hydroxyl • DFT calculations • density of states • 2D magnets • spintronics

Graphene, a two-dimensional (2D) layer of  $sp^2$ -bonded carbon atoms arranged in hexagons, has attracted continuous attention of the scientific community over the past decade owing to its exceptional mechanical, electric, transport, and optical properties, which stem from its peculiar atomic organization and electronic structure.<sup>1,2</sup> It has been successfully tested in or proposed for a broad spectrum of applications<sup>3</sup> in various fields, such as electronics,<sup>4</sup> generation and storage of energy,<sup>5,6</sup> optics,<sup>7</sup> medicine,<sup>8</sup> printing technologies,<sup>9</sup> treatment of the environment,<sup>10</sup> and mechanical reinforcements.<sup>11</sup> However, despite its unique physical features, several drawbacks have been identified that hamper its use for specific processes and utilization. They include its high hydrophobicity, zero bandgap, and lack of magnetic response. In many cases, functionalization has been shown to be an effective strategy for overcoming these drawbacks.<sup>12</sup> For instance, it has been used to synthesize a number of graphene derivatives, such as graphene oxide,<sup>13</sup> graphane,<sup>14</sup> fluorographene<sup>15,16</sup> and other halogenated graphenes,<sup>17</sup> thiographene,<sup>18</sup> cyanographene,<sup>19</sup> graphene acid<sup>19,20</sup> and hydroxographene,<sup>21</sup> significantly extending the application potential of graphene-based materials and providing attractive/competitive alternatives in fields where pristine graphene fails.

More than two decades ago, it was theoretically suggested that in a single layer of graphite, intrinsically diamagnetic, localized magnetic moments may emerge if an  $sp^3$ -type defect is formed in the hexagonal carbon lattice. Since the first isolation of graphene in 2004,<sup>1</sup> the introduction of defects has become accepted as a promising way to endow graphene with magnetic properties it lacks.<sup>22,23</sup> In general, defects formed or introduced in the graphene lattice are of diverse nature, *e.g.*, they can emerge due to (i) structural/topological disorders, such as point and line defects (*i.e.*, vacancies, interstitial atoms, periodically repeating pentagonal-heptagonal or pentagonal-octagonal motifs) and Thrown-Stone-Wales defects,<sup>24,25</sup> (ii) substitutional non-carbon atoms (*i.e.*, nitrogen, boron, sulphur),<sup>26,27</sup> (iii) adatoms (*i.e.*, light atoms such as hydrogen, fluorine, *etc.*),<sup>28-32</sup> (iv)

functionalizing groups,<sup>33,34</sup> and (v) special edge architectures and related confinement effects.<sup>35,36</sup> The presence of defects substantially modifies the electronic structure of graphene, resulting in evolution of mid-gap states or flat bands appearing at or in close proximity to the Fermi level. Most importantly, these new band features are spin polarized, implying they are associated with increased magnetic moments due to defect-promoted formation of unpaired electrons that no longer participate in bonding.

As graphene can be regarded as a bipartite system with two interpenetrating triangular lattices, the relative positions of the magnetic moments determine the type of the magnetic ground state according to the Lieb's theorem.<sup>37</sup> The generated magnetic moments, alternatively termed paramagnetic centers, may interact with each other once a communication medium is available. As a result, ferromagnetic and/or antiferromagnetic ordering can develop with sustainability against thermal fluctuations up to a finite temperature determined by the strength of the magnetic interactions among the defect-induced magnetic moments. Originally, the conductive  $\pi$ -electron system of graphene was proposed as a mediator of magnetic coupling with attributes resembling those of the Ruderman-Kittel-Kasuya-Yosida (RKKY) interaction.<sup>22,23</sup> Thus, the concept of the Stoner magnetism is sometimes adopted to account for magnetic ordering in graphene mediated by itinerant  $\pi$ -electrons occupying narrow bands at the Fermi level. However, it has often been argued, from both theoretical and experimental standpoints, that the  $\pi$ -electron system of graphene is generally too weak for maintaining the magnetic coupling over the whole structure at elevated temperatures.<sup>23,38</sup> It has also been shown that in the case of doping, the magnetic ordering can resist thermal disruption to some extent depending on the chemical nature of the dopant, its electronic features (*i.e.*, n-/p-type), its concentration and configurations of foreign atoms in the graphene lattice.<sup>26,27</sup> In such cases, the magnetic transition temperatures can be up to 100 K. In cases where

room temperature magnetic ordering has been observed, it has been heavily questioned due to the highly probable or lately confirmed presence of impurities of d-block elements stemming from the synthesis itself or sample handling.<sup>39,40</sup>

Recently,  $sp^3$  functionalization of a graphene sheet has been identified as an effective approach to induce huge magnetic moments at low temperatures.<sup>41</sup> In addition, suitable  $sp^3$  functionalization promotes the formation of a new type of the magnetic centers in graphene, known as diradical motifs, as demonstrated very recently by Tuček *et al.*,<sup>33</sup> whereas previous concepts have heavily relied on monoradical-(defect-)induced magnetism. These diradical motifs are believed to emerge only above the site percolation limit of the graphene lattice, *i.e.*, when the number of  $sp^3$ -carbon atoms is sufficient to encage the remaining  $sp^2$ -conjugated islands. In other words,  $sp^3$  functionalization must reach a defined level for both the generation of diradical motifs and suppression of lateral diffusion of adatoms that ruin the periodic pattern of  $sp^2$  magnetic islands over the graphene sheet. Most importantly, apart from acting as sources of magnetic moments, the functionalizing groups enable bridging among the diradical motifs, eventually mediating interaction among them and stabilizing the magnetic order throughout the whole graphene lattice up to high temperatures.

In particular, hydroxofluorographenes with an appropriate F/OH ratio are examples of such  $sp^3$ -functionalized graphene platforms where –OH groups act as a driving force for establishing diradical motifs by supporting their stabilization and allowing communication *via* superexchange interactions.<sup>33</sup> Although these systems show a ferromagnetic ground state, they undergo transition to an antiferromagnetic regime upon heating, which is stable up to room temperature. In other words, superexchange interactions seem to be much stronger than the  $\pi$ -electron system of graphene at maintaining the magnetic ordering to exceptionally high temperatures. Thus,

development of the functionalization approach to generate ferromagnetic ordering sustainable up to room temperature *via* strengthening the role of itinerant  $\pi$ -electrons and, at the same time, synergistic effect of other magnetic exchange mechanisms remains a challenging task.

In this work, we report a simple synthetic strategy based on the chemistry of fluorographene to prepare hydroxyl- and fluoro-functionalized 2D graphenes with super-organization of zig-zag  $sp^2$  carbon chains/paths inside an otherwise  $sp^3$ -bonded lattice. The prepared graphene derivative exhibited room temperature ferromagnetic ordering stemming from the synergistic interplay between itinerant  $\pi$ -electrons and superexchange interactions mediated by  $-OH$  groups. The synthesis of a ferromagnetic non-metallic carbon-based material could stimulate an interest in exploiting such 2D systems for advanced applications in various fields of electronics, biomedicine, spintronic, targeted delivery, and separation processes.

## RESULTS AND DISCUSSION

To prepare a magnetically ordered graphene derivative, we synthesized graphene containing zig-zag  $sp^2$  motifs embedded in an otherwise  $sp^3$  lattice with a suitable functional group that enabled magnetic interaction among the individual zig-zag motifs.<sup>42</sup> We employed a fluorographene chemistry, which allowed tailored functionalization of graphene and preparation of a wide portfolio of graphene derivatives.<sup>43-45</sup> We chose  $-OH$  groups as a functionality for establishing efficient magnetic interaction among magnetic centers embedded in the graphene lattice.<sup>33</sup> We reacted fluorographene with KOH in ethanol at an elevated temperature (see Figure 1a and Figure S1 in the Supporting Information) to prepare hydroxofluorographene (denoted thereafter as

G(OH)F) and found that it exhibited ferromagnetic ordering sustainable up to room temperature (see below).

X-ray photoelectron spectroscopy (XPS) analyses performed on as-formed G(OH)F revealed the presence of only carbon, fluorine, and oxygen, as can be seen in the XPS survey spectrum in the inset of Figure 1b. The content of these elements was 65.8%, 21.9%, and 12.3%, respectively, giving a total chemical composition of  $C_{18}(OH)_{34}F_6$ . The high proportion of oxygen in the material was also reflected in the ratio between the C–OH and various C–F bonds in high-resolution C 1s XPS (see Figure 1b) pattern. The high-resolution O 1s XPS pattern also showed that oxygen in the sample was mostly present as hydroxyl groups (see Figure S2a in the Supporting Information). The low amount of oxygen as carbonyl/carboxyl groups was probably due to the harsh reaction conditions. Quantification of various metals as potential magnetic contaminants was carried out by inductively coupled plasma mass spectrometry (ICP-MS) technique (see Table S1 in the Supporting Information). The ICP-MS analysis confirmed that the mass amounts of Fe, Ni, and Co were below 15 ppm. If the determined mass amounts of Fe, Ni, and Co and the magnitudes of their magnetic moments were considered, the total mass magnetic susceptibility ( $\chi_{\text{mass}}$ ) of these *d*-block elements was estimated to be of the order of  $10^{-8}$  emu  $\text{g}^{-1}\text{Oe}^{-1}$  at 0 K under a 1 kOe field. Since the measured  $\chi_{\text{mass}}$  values for the G(OH)F sample were of the order of  $10^{-5}$  to  $10^{-6}$  emu  $\text{g}^{-1}\text{Oe}^{-1}$  under a 1 kOe field (see below), the contribution of Fe, Ni, and Co to the sample's  $\chi_{\text{mass}}$  was assumed negligible and not responsible for the observed magnetic phenomena.

The Raman spectrum of G(OH)F (see Figure S2b in the Supporting Information) exhibited typical features of functionalized graphenes, *i.e.*, a D-band at  $1323\text{ cm}^{-1}$ , G-band at  $1608\text{ cm}^{-1}$ , and an  $I_D/I_G$  intensity ratio of 1.22. The Fourier-transform infrared (FT-IR) spectrum of G(OH)F (see Figure 1c) showed dominant peaks at  $1105$  and  $1044\text{ cm}^{-1}$  typical of a C–C–O asymmetric stretching mode

and also a peak at  $1385\text{ cm}^{-1}$  assigned to O–H bending. Finally, characteristic peaks of a C–F bond at  $1200\text{ cm}^{-1}$  and aromatic C=C bond at  $1596\text{ cm}^{-1}$  were observed along with minor signs of a C=O bond at  $1725\text{ cm}^{-1}$  in accordance with the XPS results.

High-resolution transmission electron microscopy (HRTEM) images demonstrated the existence of relatively large sheets of G(OH)F with length and widths exceeding  $1\ \mu\text{m}$  (see Figure 1d). Moreover, the sheets were observed to have a few-layered character as also confirmed by atomic force microscopy (AFM) topology and AFM height profile evidencing for a sheets' thickness of  $\sim 1.1\text{ nm}$  (see Figure S3 in Supporting Information). In the energy-dispersive X-ray spectroscopy (EDS) pattern, only peaks belonging to carbon, oxygen, and fluorine were detected (see inset in Figure 1d). No traces of other elements were observed, in agreement with the XPS analysis. More importantly, from aberration-corrected scanning transmission electron microscopy (STEM) imaging, a periodic pattern could be seen with an appearance closely resembling the expected zig-zag motifs (see Figure 1e). Thus, it seems that at such an F/OH ratio, a peculiar organization of –OH groups and –F adatoms favors formation of  $sp^2$  zig-zag chains separated by  $sp^3$  strips (see scheme in Figure 1e). This was found to be crucial not only for the emergence of magnetic ordering in G(OH)F but also for its sustainability at exceptionally high temperatures, as we shall discuss below.

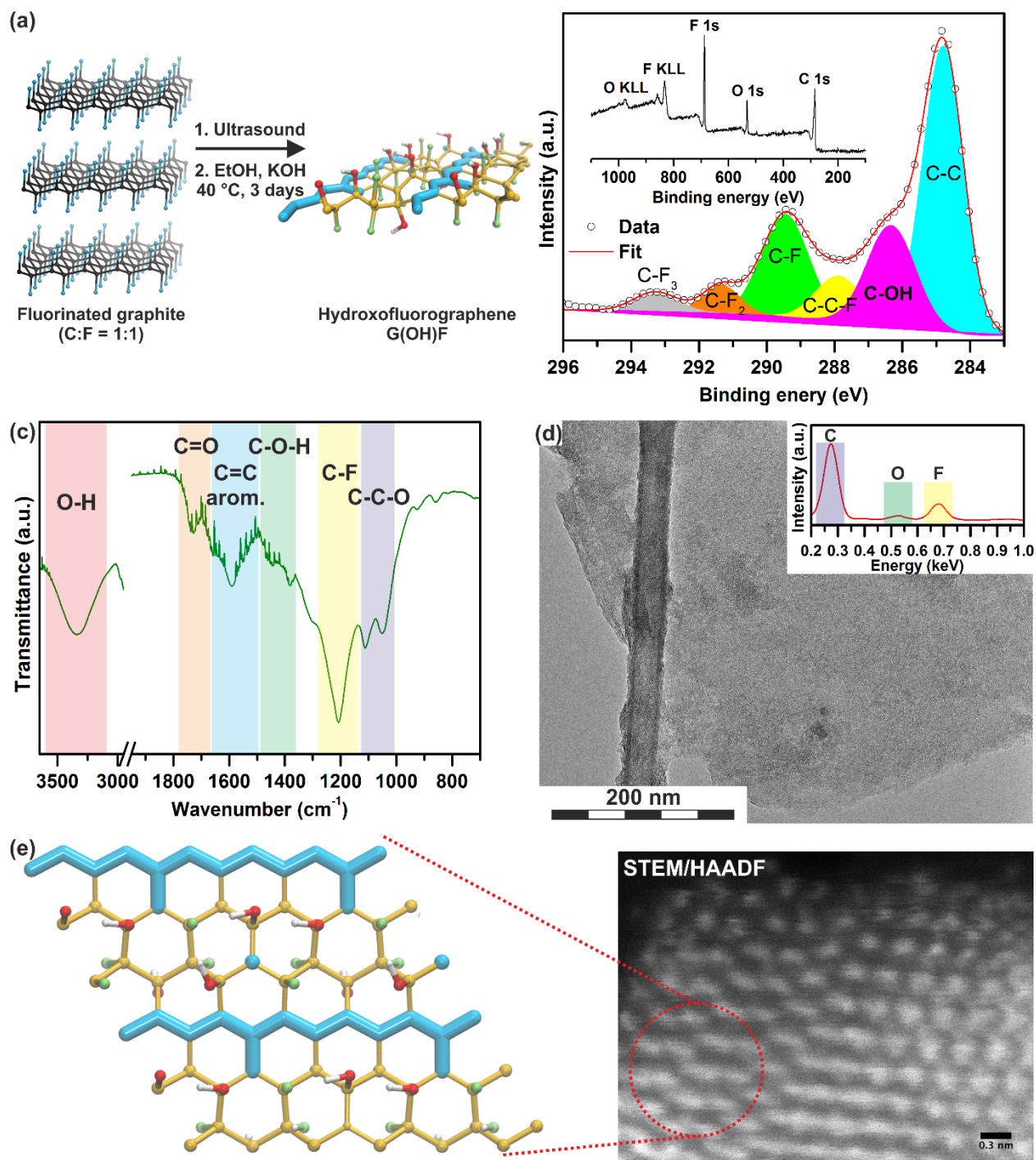


**Figure 1. Physicochemical characterization of the G(OH)F system.** (a) Schematic of the synthetic protocol for preparing G(OH)F. (b) High-resolution C 1s XPS pattern of G(OH)F with bonds indicated. The inset shows the survey XPS pattern of G(OH)F with element peaks indicated.

(c) FT-IR spectrum of G(OH)F with bands corresponding to the significant bonds marked. (d) Representative HRTEM image of a G(OH) sheet. The inset shows the EDS pattern, which confirms that only carbon, fluorine, and oxygen were present in the system. (e) Scanning transmission electron microscopy/high-angle annular dark-field imaging (STEM/HAADF) image (right) of a thin region near the edge of a G(OH)F aggregate, with evident zig-zag patterning in agreement with the model representation of zig-zag routes in the structure of G(OH)F (left).

To assess the magnetic features of the G(OH)F system, its  $\chi_{\text{mass}}$  as a function of temperature was first measured (see Figure 2a). It is well known that when defects, of whatever nature, are introduced into graphene, unpaired spins emerge with evolution of localized magnetic moments that can communicate with each other *via* charge carriers ( $\pi$ -electrons, holes) and/or exchange interactions.  $\chi_{\text{mass}}$  of the defected graphene can then be expressed by (Equation 1)

$$\chi_{\text{mass}} = \chi_{\text{mass,dia}} + \chi_{\text{mass,para}} + \chi_{\text{mass,ferro/antiferro}}, \quad (1)$$

where  $\chi_{\text{mass,dia}}$  is a diamagnetic term involving orbital, Landau and core diamagnetic contributions,  $\chi_{\text{mass,para}}$  is a paramagnetic term including a Curie-like response of non-interacting (isolated) defect-induced paramagnetic centers, paramagnetic Pauli contribution from the conduction electrons and paramagnetic van Vleck contribution, and  $\chi_{\text{mass,ferro/antiferro}}$  represents the ferromagnetic/antiferromagnetic term appearing only when the interaction among the defect-induced paramagnetic centers becomes feasible. As shown in Figure 2a,  $\chi_{\text{mass}}$  exhibited complex temperature-dependent behavior with a dramatic drop in values above  $\sim 375$  K, indicating the onset of a magnetic transition. From the second derivative of  $\chi_{\text{mass}}$ , an inflection point ( $T_{\text{inf}}$ ) was identified at a temperature of  $\sim 383$  K, which

is a characteristic signature of ferromagnetic materials when passing from a ferromagnetic state to a paramagnetic regime upon warming.

To mathematically analyze the  $\chi_{\text{mass}}$  profile recorded for the G(OH)F system, several assumptions were adopted to relate the temperature evolution of the individual contributions to the sample's  $\chi_{\text{mass}}$ . On a phenomenological level,  $\chi_{\text{mass,para}}$  was well described by the Curie law (*i.e.*,  $C/T$ , where  $C$  is the Curie constant and  $T$  is the temperature), whereas  $\chi_{\text{mass,dia}}$  was temperature-independent with a constant negative value over the entire temperature range of the measurement. Moreover, above the inflection point,  $\chi_{\text{mass}}$  was expected to obey well the Curie-Weiss law (*i.e.*,  $C/(T - \theta)$ , where  $C$  is the Curie-Weiss constant,  $T$  is the temperature and  $\theta$  is the Weiss temperature). Assuming that  $\chi_{\text{mass,para}}$  tended to zero at high temperatures, only the Curie-Weiss law with the  $\chi_{\text{mass,dia}}$  term was used for fitting  $\chi_{\text{mass}}$  above 385 K. The analysis yielded  $\theta \approx 380$  K and  $\chi_{\text{mass,dia}} \approx -9.3 \times 10^{-6}$  emu/gOe (see inset in Figure 2a). The profile of  $\chi_{\text{mass,para}}$  was derived (see inset in Figure 2a) after subtracting  $\chi_{\text{mass,dia}}$  and assuming that the ferromagnetic contribution showed a saturation tendency at low temperatures. The temperature behavior of  $\chi_{\text{mass,ferro}}$  was obtained by subtraction of  $\chi_{\text{mass,para}}$  and  $\chi_{\text{mass,dia}}$  from the  $\chi_{\text{mass}}$  data (see inset in Figure 2a).

The measured  $\chi_{\text{mass}}$  profile confirmed the existence of a magnetically ordered fraction within the G(OH)F sheets. The positive value of  $\theta$  implies that magnetic moments, induced by partial –OH substitution of –F in fluorographene, interacted ferromagnetically among each other. Since the values of  $T_{\text{inf}}$  and  $\theta$  were, within the experimental error, nearly identical,  $T_{\text{inf}}$  was ascribed to the Curie temperature ( $T_c$ ) at which transition from a ferromagnetic to paramagnetic state occurs. Thus,  $\text{C}_{18}(\text{OH})_{3.4}\text{F}_6$  behaved in a ferromagnetic manner at room temperature. Note that the existence of a ferromagnetic ground state in hydroxofluorographene systems is due to the presence and peculiar organization of diradical-based motifs. Importantly, no transition from a ferromagnetic to

antiferromagnetic state was observed for the studied  $C_{18}(OH)_{3.4}F_6$  system with zig-zag architecture, playing a crucial role in preservation of the ferromagnetic ground state up to high temperatures, as shown by theoretical calculations below.

The temperature sustainability of the ferromagnetic behavior was further evidenced from measuring and analyzing hysteresis loops for the G(OH)F system recorded over the temperature range from 5 to 400 K (see Figure 2b-d and Figure S4 in the Supporting Information). At 5 K, the magnetization vs. field curve showed a complex profile with a diamagnetic profile dominating at high applied magnetic fields and hysteresis trend at low external magnetic fields. After subtracting the diamagnetic component, the isothermal magnetization curve featured contributions from both the paramagnetic and ferromagnetic fraction in the G(OH)F sheets (see inset in Figure 2b). Note the relatively high value of coercivity amounting to  $\sim 320$  Oe (see inset in Figure 2b), which implies that the magnetic anisotropy within the G(OH)F structure holding the magnetic moments in preferential orientations is favored by the 2D character of the G(OH)F sheet, organization of magnetic motifs and interactions between them.

Upon increasing the temperature, the hysteresis profile of the isothermal magnetization curves persisted (see Figure 2c,d and Figure S4 in the Supporting Information). However, although the coercivity of the ferromagnetic fraction gradually decreased (see inset in Figure 2d), it did not strictly follow the function valid for the expected magnetic response from defect-induced localized magnetic moments. This signifies a different nature of the magnetic moments, *i.e.*, similar to diradical-based motifs, as previously proposed for hydroxofluorographene systems with an  $sp^3/(sp^2 + sp^3)$  ratio over the percolation limit,<sup>33</sup> and complex temperature behavior of magnetic anisotropy associated with the magnetically-active patterns. Most importantly, the hysteresis was observed even at 300 K (see Figure 2b) with a coercivity value of  $\sim 105$  Oe, further confirming the stability

of the ferromagnetic fraction up to room temperature. The hysteresis was lost between 375 and 400 K, implying transition to a paramagnetic regime, in accordance with the  $\chi_{\text{mass}}$  data; at 400 K, the isothermal magnetization curve exhibited only the diamagnetic and paramagnetic profiles (see Figure 2d and Figure S4 in the Supporting Information). The hysteresis loops collected for  $\text{C}_{18}(\text{OH})_{3.4}\text{F}_6$  in the temperature range from 5 to 400 K displayed a notable diamagnetic contribution. Such a feature can be explained by the presence of a significant number of itinerant  $\pi$ -electrons in  $\text{C}_{18}(\text{OH})_{3.4}\text{F}_6$ , which orbit around the benzene rings in the lattice similarly to those in ideal, defect-free graphene. This suggests that the itinerant  $\pi$ -electrons might assist in the interaction mechanism with superexchange interactions, encouraging the persistence of a ferromagnetic ground state against the temperature.

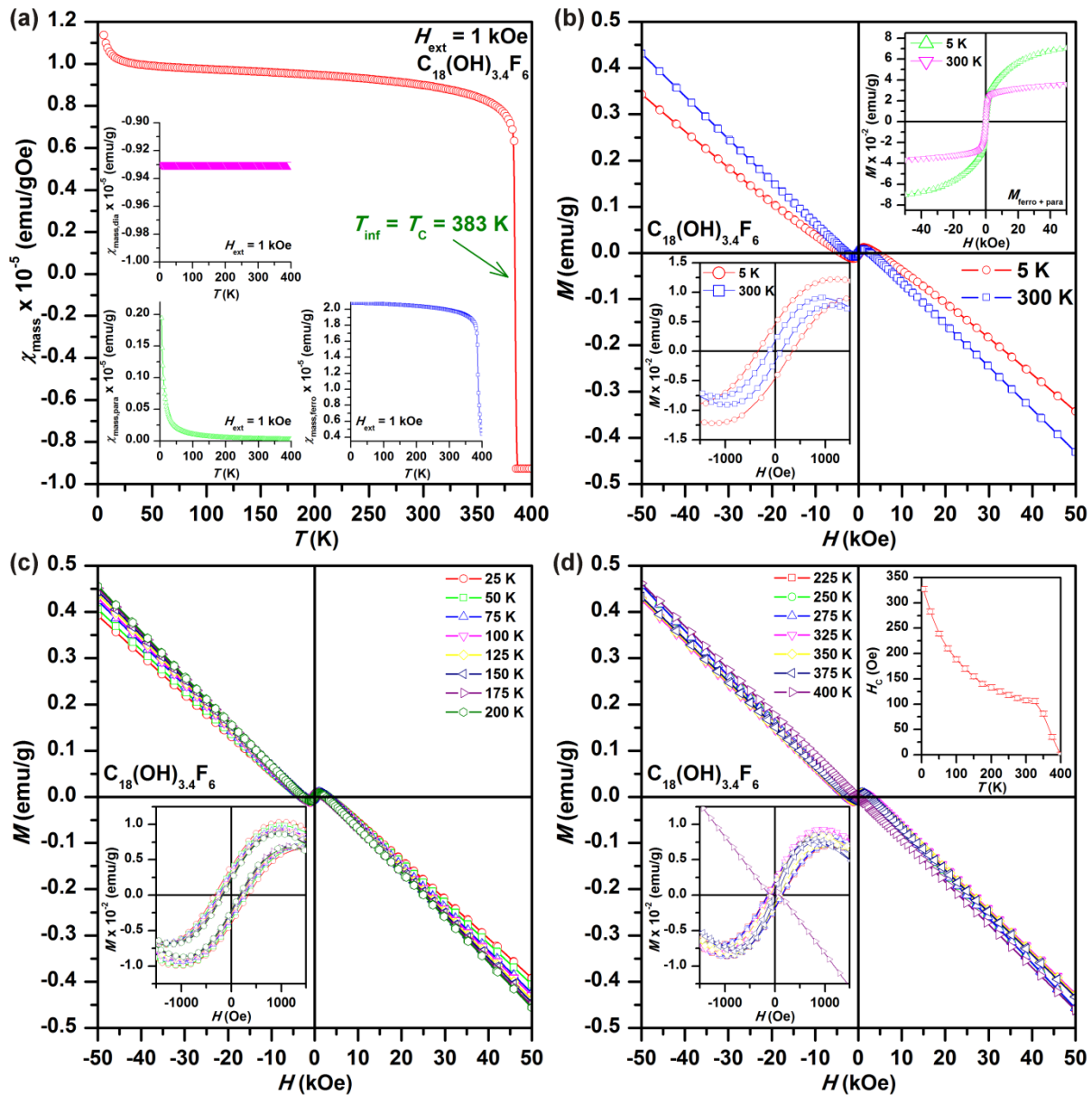


**Figure 2. Magnetization measurements of the G(OH)F system.** (a) Temperature evolution of the mass magnetic susceptibility ( $\chi_{\text{mass}}$ ) recorded for the  $\text{C}_{18}(\text{OH})_{3.4}\text{F}_6$  sample under an external magnetic field ( $H_{\text{ext}}$ ) of 1 kOe. The insets show the profile of the diamagnetic ( $\chi_{\text{mass,dia}}$ ), paramagnetic ( $\chi_{\text{mass,para}}$ ), and ferromagnetic ( $\chi_{\text{mass,ferro}}$ ) contribution to the total  $\chi_{\text{mass}}$  obtained from analysis of the  $\chi_{\text{mass}}$  plot.  $T_{\text{inf}}$  and  $T_{\text{c}}$  correspond to the temperature of the inflection point and Curie temperature, respectively, and indicate transition from a ferromagnetic state to paramagnetic regime upon warming the

sample in the chamber of the magnetometer. (b) Hysteresis loops ( $M$  vs.  $H$  curves) of the  $C_{18}(OH)_{3.4}F_6$  sample measured at a temperature of 5 and 300 K. The lower inset shows the behavior of the isothermal magnetization curves around the origin, providing evidence for non-zero values of the coercivity and remanent magnetization. The upper inset displays hysteresis loops after subtraction of the diamagnetic part ( $M_{\text{ferro} + \text{para}}$  denotes the magnetization of the ferromagnetic and paramagnetic fraction together). (c) Hysteresis loops ( $M$  vs.  $H$  curves) of the  $C_{18}(OH)_{3.4}F_6$  sample at a temperature of 25 and 200 K. The lower inset shows the behavior of the isothermal magnetization curves around the origin, providing evidence for non-zero values of the coercivity and remanent magnetization. (d) Hysteresis loops ( $M$  vs.  $H$  curves) of the  $C_{18}(OH)_{3.4}F_6$  sample measured at temperatures from 225 and 400 K. The lower inset shows the behavior of the isothermal magnetization curves around the origin, providing evidence for non-zero values of the coercivity and remanent magnetization. The upper inset displays the temperature dependence of the coercivity ( $H_c$ ), derived from the respective hysteresis loops.

Electron paramagnetic resonance (EPR) spectroscopy was used as a complement to the bulk mass magnetic susceptibility analysis and allowed further probing of the nature and dynamics of the spin species in the high temperature region (100–300 K) where the anomalous  $\chi_{\text{mass}}$  behavior was evident (see Figure 3 and related Figures S5–S23 in the Supporting Information). The X-band EPR spectrum of powder  $C_{18}(OH)_{3.4}F_6$  recorded at 113 K is shown in Figure 3a. This material exhibited a resonance signature consistent with an organic based radical very different from the EPR spectrum of the commercial fluorographene ( $C_1F_{1.1}$ ) precursor (see Figure 3c). The observed signal for  $C_{18}(OH)_{3.4}F_6$  did not show  $g$ -anisotropy nor  $^{19}\text{F}$  and  $^1\text{H}$ -hyperfine splitting associated with soluble OH residues from the starting potassium hydroxide. Instead, it exhibited only a narrow EPR signal

( $\Delta B_{pp} = 0.482$  mT) centered at  $g_{\text{eff}} = 1.9971(1)$  (validated against  $\text{Mn}^{2+}\text{MgO}$  standard) (see Figure S6 and Figures S9–17 in the Supporting Information). Resonance signals ascribable to other soluble paramagnetic species/contaminants were not detected in the broad range (see Figure S5 in the Supporting Information). The absence of Dysonian-shaped signals,<sup>46,47</sup> which are known to be associated to itinerant spins, in conduction electron spin resonance (CESR) spectroscopy indicated that the spins were localized in  $\text{C}_{18}(\text{OH})_{3,4}\text{F}_6$ . The integrated  $\text{C}_{18}(\text{OH})_{3,4}\text{F}_6$  resonance signal was well described by the Voigt shape function (see Figure S7 in the Supporting Information), similar to the findings of Rao *et al.*<sup>48</sup> in ultra-small double-walled carbon nanotubes embedded in zeolite, but with dominant Lorentzian character ( $W_G$ , Gaussian-weight of  $2.33 \times 10^{-5}$  and  $W_L$ , Lorentzian-weight equal to 0.90).

The narrow peak-to-peak line width indicates that the unpaired electrons collectively experience the fast exchange regime, known as the exchange narrowing effect. Such a phenomenon stems from the occurrence of exchange interactions among unpaired electrons ( $H_{\text{ex}}$ ) with strength large enough to yield a random frequency modulation. When  $H_{\text{ex}} \gg H_{\text{dip}}$ , where  $H_{\text{dip}}$  corresponds to dipolar interactions arising from radical centers in close space proximities, the effect on the spin system due to frequency modulation is to average out the dipolar interactions. Hence, the resonance line associated with the entire spin packets approaches that of the isolated, non-interacting electron spin moment. The observation of an electronic transition at half-field (around  $g \approx 4$ ; see Figure S8 in the Supporting Information) further indicates that the radical system description is under a strong exchange regime.

Theoretically, the effect of exchange narrowing has been elucidated by van Vleck, Kubo and Tomita, and by Andersson.<sup>49–52</sup> From the EPR spectrum shown in Figure 3a, the spin-spin relaxation time ( $T_2$ ) was estimated using the relation (Equation 2)

$$T_2 = 1/\gamma \Delta\nu_L, \quad (2)$$

where  $\Delta\nu_L = (2/\sqrt{3})\Delta B_L$  and  $\Delta B_L$  corresponds to the peak-to-peak field width (in magnetic units) of the unsaturated Lorentzian line. The calculated  $T_2$  value was  $1.36 \times 10^{-8}$  s for  $C_{18}(OH)_{3.4}F_6$ . This value is much smaller than that estimated for neat fluorographene ( $T_2$  of  $2.6 \pm 10^{-5}$  s) by Panich *et al.*<sup>53</sup> The temperature dependence of the EPR signals of  $C_{18}(OH)_{3.4}F_6$  recorded in the range of 113–253 K did not show changes from the Voight-shape resonance profile, appreciable changes in the peak-to-peak width ( $\Delta B_{pp}$ ) or any spread in  $g_{\text{eff}}$  (see Figures S8–16 in the Supporting Information). Figure 3d presents experimental values determined for  $g_{\text{eff}}$  vs.  $T$  (lower panel) and  $\Delta B_{pp}$  vs.  $T$  (upper panel) from linear fitting analysis (red-line;  $\Delta B_{pp} = 4.82 \pm 0.01$  Gauss, slope equals to  $8.3 \times 10^{-5}$ ;  $g_{\text{eff}} = 1.9970 \pm 0.0001$ , slope equals to  $1.69 \times 10^{-9}$ ).

The variation of the spin-population of  $C_{18}(OH)_{3.4}F_6$  recorded as a function of the temperature is shown in Figure 3b ( $\chi_{\text{EPR}} \times T$  vs.  $T$ , with  $T$  from 113 to 253 K), where the term  $\iint d\chi_{\text{EPR}}$  represents the double integrated EPR signal intensity recorded at a fixed microwave power (0.1 mW). The observed increase of the spin-population shows a clear departure from Curie-like behavior. Hence, the trend is not consistent with that expected for paramagnetic species. This is consistent with the abovementioned  $\chi_{\text{mass}}$  data. The clear increase of the  $\chi_{\text{EPR}} \times T$  product shows that the unpaired electrons must be correlated together *via* exchange interactions and the correlation is ferromagnetic in nature. To gain further understanding of the system spin dynamics, power saturation experiments were performed at four selected temperatures. The saturation results are shown in Figure 3f. Figure 3e shows, as an example, the evolution of the  $C_{18}(OH)_{3.4}F_6$  EPR signals recorded at 133 K as a function of increasing microwave power (from 0.05 mW to 32 mW, drawn as a simple superimposition) to investigate the possible effect of itinerant electrons on the magnetic

regime. Results from other experiments at various temperatures and microwave powers are shown in Figures S18–23 in the Supporting Information.

To analyze the saturation trends, first-derivative EPR spectra recorded at different microwave powers ( $P$ ), were fitted using Portis and Castner's theory (Equation (3)):<sup>54,55</sup>

$$\iint S = \frac{k \times \sqrt{P}}{[1 + (P/P_{1/2})]^{b/2}},$$

(3)

where the term  $\iint S$  indicates the double integrated signal intensity,  $P$  is the applied microwave power,  $b$  is the relaxation factor ( $b = 1$  for inhomogeneous line broadening (Gaussian line) and  $b = 3$  for homogeneous line broadening (Lorentzian line)),  $P_{1/2}$  is the power at which the signal is half-saturated, and  $k$  is an experimental constant associated to the instrument. From global fitting analysis, a (spin correlated)  $b$  value of  $0.62 \pm 0.01$  was obtained for all the microwave powers and temperatures examined. The  $P_{1/2}$  value, which was  $\propto 1/T_1T_2$ , showed a strong dependence on the sample temperature. In the high temperature regime ( $T = 253$  K),  $P_{1/2}$  was rather large, with a half-saturation value of  $2.283 \pm 0.102$  mW. At lower temperatures, there was a sudden drop in the half-saturation value, which became nearly temperature independent ( $P_{1/2}$  of  $0.544 \pm 0.061$  mW at 213 K;  $P_{1/2}$  of  $0.427 \pm 0.124$  mW at 173 K;  $P_{1/2}$  of  $0.317 \pm 0.030$  mW at 133 K). Since the relaxation factor  $b$  converges to less than 1, laying outside the region of uncorrelated spins, a fast exchange regime of the collective spin system in  $C_{18}(\text{OH})_{3,4}\text{F}_6$  is therefore validated.

Taking together the results from bulk  $\chi_{\text{ms}}$  and the EPR analyses, the present findings can be interpreted as follows. The mechanism for the appearance of magnetism in carbon based materials is widely accepted to involve C-based defects (non-bonding localized states, dangling-bonds,

states localized on edge carbon atoms), giving rise to spin-polarized  $\pi$ -electrons of carbon. However, taken together, the results from the bulk  $\chi_{\text{mass}}$  and EPR analyses indicate that in the case of  $\text{C}_{18}(\text{OH})_{3.4}\text{F}_6$ , the observed ferromagnetic interaction and power saturation trends of the fast exchange regime cannot simply be explained by strong correlation between localized spins. Spin-spin interactions in organic based materials containing strongly correlated localized spins usually show saturation values that are much larger than those observed here.<sup>56</sup> Furthermore, from Portis and Castner's theory, the  $P_{1/2}$  value cannot remain nearly constant, as observed here in the 133–213 K regime. Systems that express a CESR signal are expected to show an emergence of ( $T$  independent) Pauli-type spin susceptibility that translates into a strong dependence of the signal width in response to cooling, and a substantial  $g_{\text{eff}}$ -shift from that of the free electron value ( $g_{\text{eff}} > 2.00232$ ) due to spin-orbit coupling.<sup>57</sup> Since these effects were not observed, the recorded EPR envelope for  $\text{C}_{18}(\text{OH})_{3.4}\text{F}_6$ , together with its saturation and magnetic behavior, cannot be exclusively ascribed to conduction electrons. On the other hand, it has been reported that the occurrence of Heisenberg ( $S = 1/2$ ) chain-type interaction between localized spins mediated by itinerant spins can produce ferromagnetism in proton irradiated graphite (*i.e.*, activated carbon fibers).<sup>58,59</sup> Therefore, we suggest that a similar scenario may occur in  $\text{C}_{18}(\text{OH})_{3.4}\text{F}_6$ , *i.e.*, the observed magnetic behavior results from exchange interaction among localized spins mediated by itinerant  $\pi$ -electrons. In other words, the presence of itinerant  $\pi$ -electrons, witnessed from the magnetization and EPR measurements, implied the existence of  $sp^2$ -conductive pathways organized within the  $\text{C}_{18}(\text{OH})_{3.4}\text{F}_6$  structure. Formation of a similar  $\pi$ -electron-based conductive network was previously reported for less-fluorinated regions of fluorographene prepared by fluorination of graphene grown by chemical vapor deposition technique.<sup>60</sup> A highly inhomogeneous fluorine coverage was found to produce multilayer islands, folds, wrinkles, and ripples, all containing a lower content of

fluorine, consequently forming a conductive superstructure through which the charge transport, mediated by itinerant  $\pi$ -electrons, occurred preferentially.<sup>60</sup>

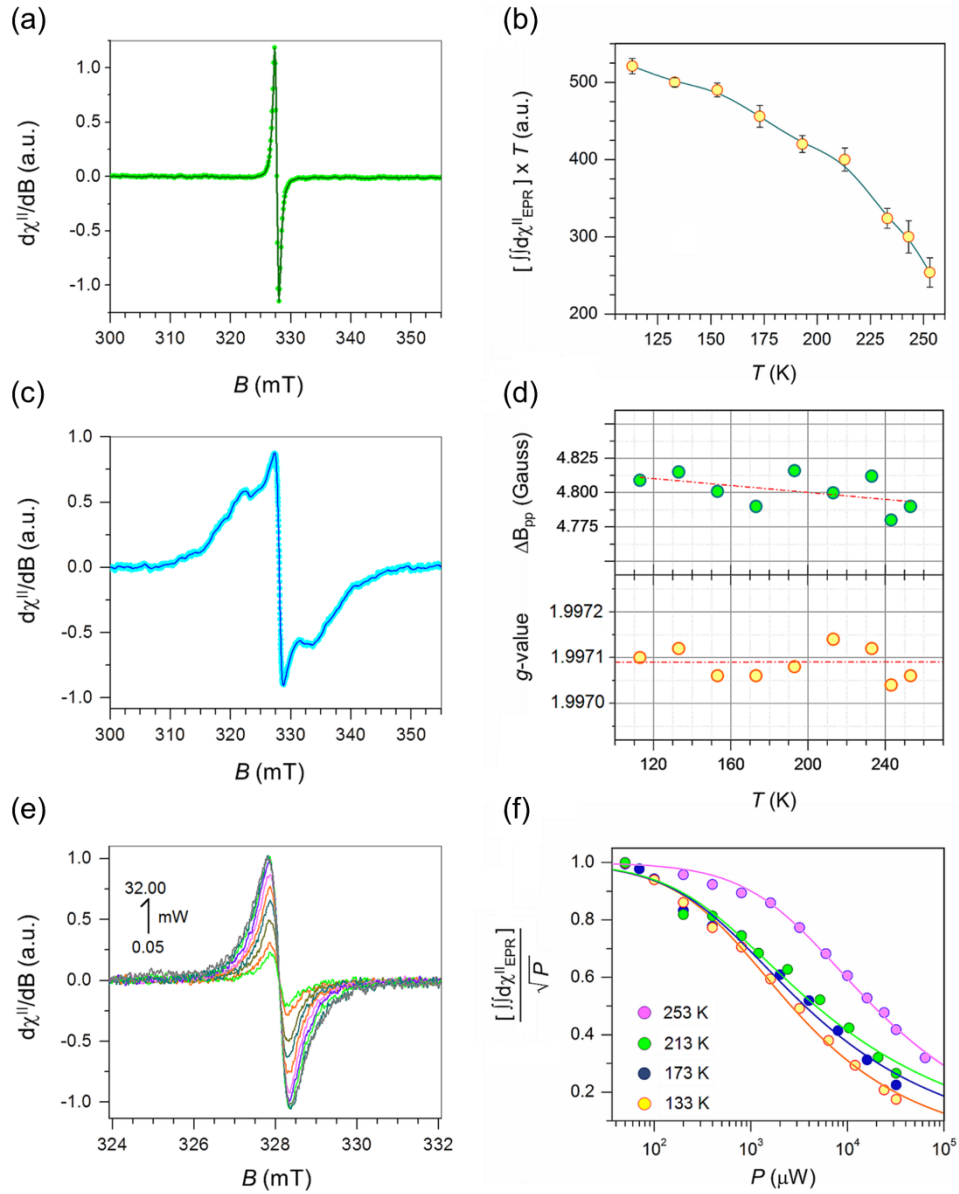


**Figure 3. EPR measurements and analyses of the G(OH)F system.** (a) X-band (9.17 GHz) EPR spectrum of  $C_{18}(OH)_{34}F_6$ , recorded at 113 K with 100 kHz modulation frequency, 0.2 mT

modulation width, 100  $\mu$ W microwave power, 4 min sweep time and 0.03 s time constant, 4 scan accumulated and averaged. (b) Temperature dependence of the spin population obtained for  $C_{18}(\text{OH})_{3.4}\text{F}_6$  (circles) plotted in the form of  $\int\int\chi_{\text{EPR}} \times T$  vs.  $T$ . (c) X-band (9.17 GHz) EPR spectrum of commercial fluorographene ( $C_1\text{F}_{1.1}$ ), recorded at 113 K with 100 kHz modulation frequency, 0.2 mT modulation width, 100  $\mu$ W microwave power, 4 min sweep time and 0.03 s time constant, 4 scan accumulated and averaged. (d) Variation of  $g_{\text{eff}}$  and peak-to-peak line width ( $\Delta B_{\text{pp}}$ ) for  $C_{18}(\text{OH})_{3.4}\text{F}_6$  recorded as a function of the sample temperature. (e) EPR power-saturation resonance signals (from 0.05 mW to 32 mW) recorded at 133 K for  $C_{18}(\text{OH})_{3.4}\text{F}_6$ . (f) Power saturation plots with values normalized to the non-saturating condition. The fitting analysis (solid-lines) results were obtained from Portis and Castner's saturation equation.

Density functional theory (DFT) calculations using  $C_{18}(\text{OH})_{3.4}\text{F}_6$  as a model (see Supporting Information for further details and respective Figure S24 and Figure S25 in the Supporting Information) with stoichiometry very close to the experimental one identified a structural motif (see Figure 4a) possibly responsible for the room temperature ferromagnetism of the  $C_{18}(\text{OH})_{3.4}\text{F}_6$  system. The motif consisted of  $sp^2$ -conjugated zig-zag chains passing through  $sp^3$  domains with radical centers that were isolated in the  $sp^3$  region and attached as a side part of the  $\pi$ -chain, as also evidenced by further STEM and electron energy loss spectroscopy (EELS) experiments (see below). The spontaneous formation of zig-zag motifs during synthesis of G(OH)F is supported by bond dissociation energies (BDEs) of fluorine atoms favoring defluorination along the motif (see Figure S26 in the Supporting Information). A transition temperature of 440 K estimated for  $C_{18}(\text{OH})_{3.4}\text{F}_6$  by using the Ising model on the honeycomb lattice<sup>61,62</sup> (see Methods Section below for

details) indicated that the ferromagnetically ordered state was stable up to temperatures exceeding 300 K, in good agreement with the experimentally derived  $T_c$ . The electronic structure displayed as density of states (DOS) of the  $C_{18}(OH)_iF_6$  model provided insights into the magnetic exchange mechanism in the G(OH)F system (see Figure 4b). The DOS of  $C_{18}(OH)_iF_6$  in the ferromagnetic state exhibited a continuum of states at the Fermi level ( $E_f$ ) predominantly composed of  $\pi$ -chain states. Importantly, the electronic states of the radicals,  $-OH$  groups and  $-F$  adatoms contributed significantly to the DOS at  $E_f$ . A complex exchange mechanism can therefore be anticipated for the ferromagnetic G(OH)F system, with both superexchange coupling of the radicals to the  $sp^2$  zig-zag chains and the  $\pi$ -electron system transferring the coupling between  $sp^3$  strips, in line with both the magnetization and EPR measurements. Theoretical calculations for close stoichiometries, *i.e.*,  $C_{18}(OH)_iF_5$  and  $C_{18}(OH)_jF_5$ , showed the same features. Thus, similar types of magnetism arise from similar structural and electronic features, demonstrating the robustness of the model in explaining the observed magnetism (see Supporting Information for further details and respective Figure S27 and Figure S28 in the Supporting Information). In summary, the theoretical calculations indicated that the magnetic ordering sustainable up to very high temperatures exceeding room temperature originated from complex-organization of radical motifs and zig-zag conjugated  $sp^2$  carbon chains embedded in  $sp^3$  functionalized graphene lattice allowing for combined contributions of superexchange interactions mediated through the F/OH functionalization and indirect exchange *via* itinerant  $\pi$ -electrons.

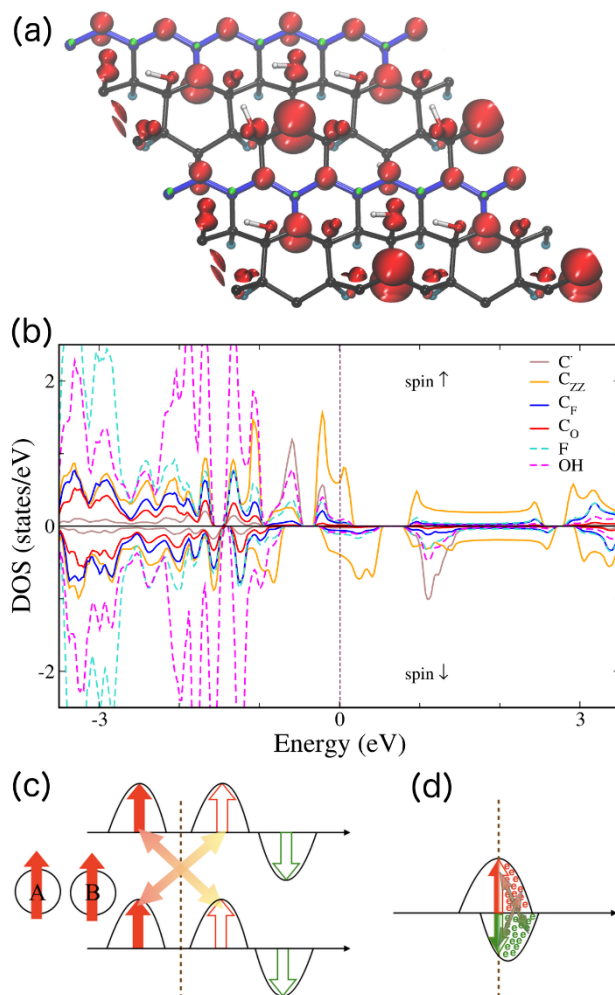


**Figure 4. Theoretical calculations performed for the G(OH)F system.** (a) Top view of the prototypical ferromagnetic  $C_{18}(OH)_4F_6$  structure (the same structure as shown in Figure 1e) with spin densities (positive shown in red and negative in green) plotted for isosurfaces at  $5 \times 10^{-3} e \text{ \AA}^{-3}$ . (b) Corresponding atom resolved spin-polarized DOS plot. The plot is zeroed at  $E_F$ . (c, d) Schematic of DOS of the two parallel-aligned magnetic moments with a ferromagnetic superexchange interaction (panel (c)) and itinerant electron magnetism, the interaction of magnetic spins mediated by conduction electrons (panel (d)).

The validity of the computational structural models was further demonstrated by STEM imaging (see Figure 5 and Supporting Information for further details), which revealed a repeating linear contrast with a periodicity close to 0.29 nm (see Figure 5c,f). Although the repeating linear contrast of the theoretical monolayer structures of G(OH)F does not directly match the experimental images (see Figure S29 in the Supporting Information), considering that the imaged area contains several layers, we simulated STEM images of bilayer G(OH)F material, which yields an apparent feature separation in a very good agreement with the experimental data (see Figure S30 in the Supporting Information). Furthermore, EELS mapping of the O *K* edge revealed the presence of oxygen, with a lineshape characteristic of –OH groups (see Figure 5e,g). Importantly, theoretical calculations showed that layering of G(OH)F does not significantly affect its electronic and magnetic features compared to single free-standing sheets (see Figure S30e in the Supporting Information), regardless of the stacking sequence of the sheets.

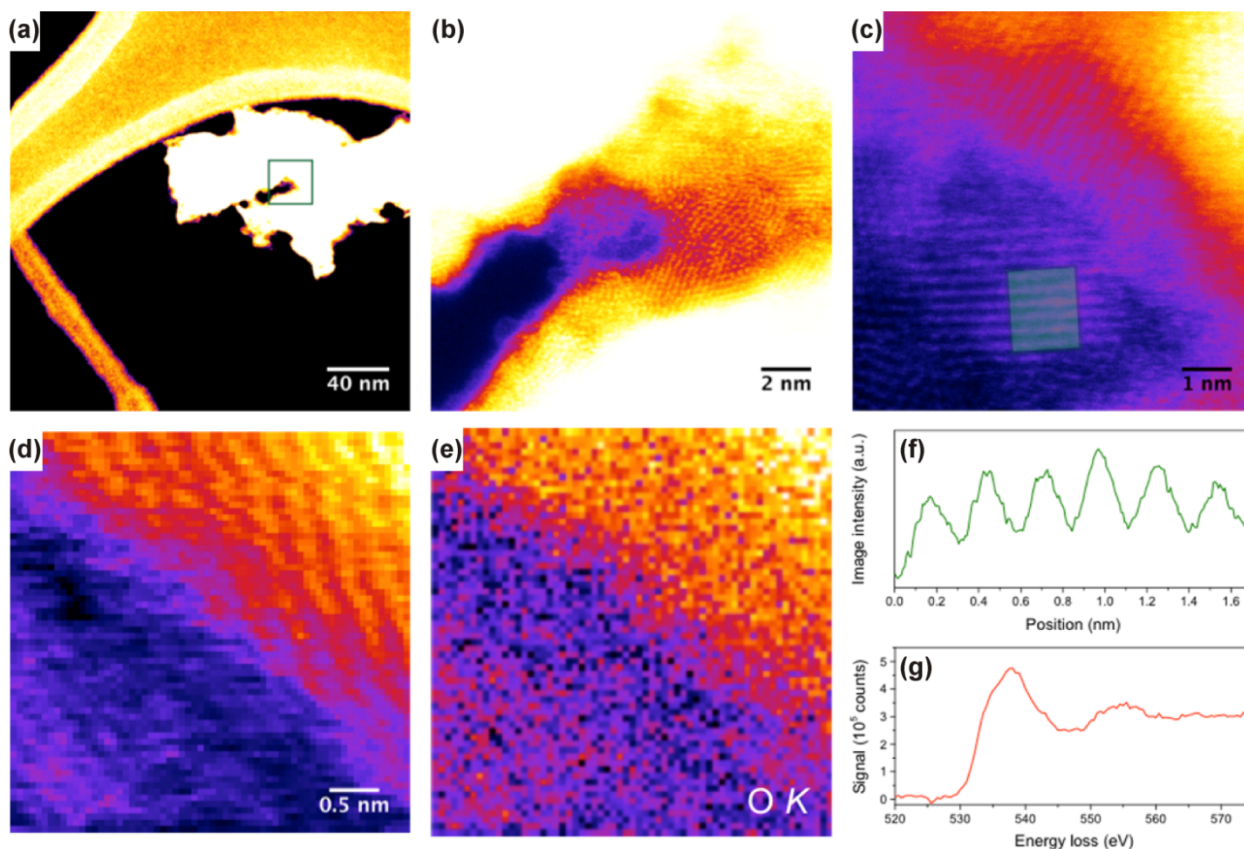


**Figure 5. STEM/EELS characterization of the G(OH)F system.** (a) STEM/MAADF image of an aggregate dispersed on a holey carbon support film. MAADF stands for medium-angle annular dark-field imaging. (b) Close-up of the region indicated by the green open square in panel (a). (c) STEM/HAADF image of a region near the left edge of that shown in panel (b). The green rectangle is overlaid on the repeating linear features and indicates the location of the line profile plotted in panel (f). (d) STEM/HAADF image recorded during a spectrum map of a region near the center of panel (c). (e) Mapped intensity of the background-subtracted EELS signal integrated over the O *K*-edge. All panels are colored with the ImageJ lookup table “Fire”. (f) Line profile perpendicular to the linear features in panel (c), with a period of 0.29 nm. (g) Background-subtracted EELS O *K*-edge spectrum integrated over panel (e), which is highly consistent with –OH chemical groups.

## CONCLUSION

In summary, we exploited the concept of functionalization for preparation of a graphene derivative showing a ferromagnetic behavior sustainable at room temperature. In particular, we focused on hydroxofluorographenes and experimentally found a member with a robust ferromagnetic ground state. It was demonstrated that for a suitable F/OH coverage of a graphene sheet, functionalization-promoted magnetic motifs – sources of magnetic moments – strongly interacted with each other to retain ferromagnetic properties up to an exceptionally high temperature of  $\sim 383$  K when the paramagnetic state became established. Theoretical calculations showed that at such an F/OH ratio, sophisticated organization of magnetic motifs emerged, consisting of  $sp^2$ -conjugated zig-zag chains passing through  $sp^3$  domains with radical centers either isolated in the  $sp^3$  region or attached as a side part of the  $\pi$ -chain. The predicted in-plane distance between the zig-zag chains was experimentally observed by high-resolution scanning transmission electron microscopy. The structural configuration in hydroxofluorographene was found to be influenced not only by the thermodynamic stability of the individual structures but also the kinetics and random organization of defects over the surface of the starting fluorographene. The favored arrangement of magnetically-active motifs strengthened interaction pathways among them *via* itinerant  $\pi$ -electrons, as demonstrated by analyses of magnetization measurements and EPR data. Such a scenario was further verified and explained by theoretical calculations, which suggested that the ferromagnetic state is maintained by a synergistic interplay between the superexchange coupling the radicals to the  $sp^2$  zig-zag chains and the  $\pi$ -electron system transferring the coupling between  $sp^2$  strips. In addition, while nucleophilic substitution promotes formation of radical centers and emergence of superexchange interactions, defluorination pathways lead to the formation of the  $sp^2$

zig-zag motif with strengthening the role of itinerant  $\pi$ -electrons as confirmed by theoretical computations.

The presented results highlight the importance of considering  $sp^2$  functionalization when designing and preparing graphene-based materials possessing  $sp$ -driven magnetism that is stable even at room temperature. Moreover, it provides many degrees of freedom in terms of the diversity of magnetic motifs, their architecture, combination and organization, allowing formation of structures with various  $sp^2/sp^3$  ratios differing in electric and magnetic properties targeted toward a given application. We believe that the presented concept will stimulate further interest and research in graphene-based organic magnets with features tunable by varying the level of  $sp^2$  functionalization. This will enable optimal structures to be identified that guarantee the emergence and temperature preservation of magnetic ordering, thus extending the application portfolio of graphene and graphene derivatives for use in spintronics, biomedicine and other related fields.

## METHODS

**Materials.** Fluorinated graphite ( $C_{60}F_{14}$ )<sub>n</sub> and potassium hydroxide (KOH) were purchased from Sigma-Aldrich. The solvents for synthesis and purification were obtained from PENTA, Czech Republic. Dialysis tubing (12.4 kDa cut off) was purchased from P-lab company (Czech Republic). All the chemical were used without further purification.

**Synthesis.** Potassium hydroxide (250 mg) was solubilized in 8 ml of ethanol overnight. Afterwards, 250 mg of fully fluorinated graphite was added and the solution was sonicated for 2 h. The formed suspension was heated to 40 °C and then stirred at this temperature for 72 h. The

resulting material was purified (see Figure S1 in the Supporting Information) by washing sequentially with aliquots of acetone (2×), ethanol (2×), and water (2×) separated by centrifugation at  $20\,000 \times g$ . The final pellet after centrifugation of the water suspension was redispersed in ethanol and centrifuged at  $3\,000 \times g$  to obtain the most hydrophilic fraction of the prepared material in the supernatant. The supernatant fraction was afterwards dialyzed against water in the dialysis tube with a 12.4 kDa cut-off for 3 days to remove residual potassium ions. The material was either lyophilized or stored as a water suspension. The yield of this very fine fraction was between 2–3%.

**Characterization Methods.** XPS measurements were performed on a PHI VersaProbe II (Physical Electronics) spectrometer fitted with an Al K<sub>α</sub> source (15 kV, 50 W) and controlled by MultiPak software (Ulvac-PHI, Inc.). The data were referenced relative to the C 1s peak at 284.80 eV.

FT-IR characterization was conducted on an iS5 Thermo Nicolet Spectrometer utilizing the Smart Orbit ZnSe ATR technique. A DXR Raman microscope with a 780 nm excitation line of a diode laser was used for Raman measurements.

An ICP-MS Agilent 7700x device was used for detection of residual metals in the prepared G(OH)F sample. Prior to the detection, 3 mg of the G(OH)F sample was kept at 100 °C in 10 mL trace metal basis nitric acid for 2 h. The insoluble residues were afterwards removed by passing through a 200 nm filter and the solution was diluted with nitric acid to 25 mL in a volumetric flask. The final solution was used as a blank sample of trace metal basis nitric acid.

A physical property measurement system (PPMS, Quantum Design, U.S.A.) equipped with a vibrating sample magnetometer (VSM) was employed for collecting magnetization data of the

G(OH)F sample. The temperature dependence of the G(OH)F sample's magnetization was measured upon warming in the temperature interval from 5 to 400 K under an external magnetic field of 1 kOe after cooling in a field of 1 kOe. Hysteresis loops of the G(OH)F sample were recorded in an external magnetic field ranging from  $-50$  to  $+50$  kOe and at various temperatures from 5 to 400 K. Prior to analysis, the magnetization values were corrected by considering the response of the sample holder, sample capsule and respective Pascal constants.

EPR spectra of the powder G(OH)F sample were recorded on a JEOL JES-X-320 spectrometer operating at the X-band frequency ( $\sim 9.14$ – $9.17$  GHz) equipped with a variable temperature control ES 13060DVT5 apparatus. The cavity  $Q$  quality factor was kept above 6000 in all the measurements. Highly pure quartz tubes were employed (Suprasil, Wilmad,  $\leq 0.5$  OD) and accuracy on  $g$ -values was obtained against an  $\text{Mn}^{2+}/\text{MgO}$  standard (JEOL standard).

HRTEM images were obtained and STEM/HAADF analyses for EDS mapping of elemental distributions on the G(OH)F sample were performed with a FEI TITAN 60-300 HRTEM device equipped with an extreme field emission gun (X-FEG) electron source operating at 80 kV. For the HRTEM, STEM-HAADF and EDS experiments, an aqueous solution of the G(OH)F sample at a concentration of  $0.1 \text{ mg mL}^{-1}$  was redispersed by ultrasonication for 5 min. A drop of the sonicated sample was then deposited on a carbon-coated copper grid and slowly dried at laboratory temperature for 24 h to reduce its content of adsorbed water. The G(OH)F sample for AFM measurements was prepared following the protocol identical for HRTEM, STEM-HAADF and EDS experiments; the solution was just deposited on a mica substrate and the AFM measurements were performed on an NTEGRA Aura instrument.

The G(OH)F sample was further imaged in an aberration-corrected Nion UltraSTEM100 scanning transmission electron microscope operated at an acceleration voltage of 60 kV. The beam current was around 50 pA, the beam convergence semi-angle was 30 mrad and the detector angular ranges were 60–200 mrad for MAADF option and 80–300 mrad for HAADF option. Images were colored with the ImageJ lookup table "Fire" to highlight relevant details. Core-loss EELS was performed on the same instrument using a Gatan PEELS 666 spectrometer retrofitted with an Andor iXon 897 electron-multiplying charge-coupled device (EMCCD) camera.<sup>63</sup> The energy dispersion was 0.1 eV/pixel (with an instrumental broadening of 0.4 eV) and the EELS collection semiangle was 35 mrad.

To simulate STEM images, we used the PyQSTEM interface<sup>64</sup> to the Quantitative TEM/STEM Simulations (QSTEM) code.<sup>65</sup> The model structures were first relaxed with density functional theory, and then MAADF or HAADF images were simulated using our experimental STEM parameters, with scattering potentials described using the independent atom approximation.<sup>66</sup>

**Computational Methods.** *Plane-Wave (PW) Density-Functional-Theory (DFT) Calculations with Periodic Boundary Condition (PBC).* DFT-PBC computations were performed using the Vienna *ab initio* simulation package (VASP)<sup>67</sup> employing the Perdew, Burke, and Ernzerhof (PBE)<sup>68</sup> exchange and correlation functional and projected augmented wave potentials (PAW)<sup>69,70</sup> to represent atomic cores. The wave functions were expanded in the PW basis set with a cutoff of 500 eV. Brillouin zone integrations were performed with an  $11 \times 11 \times 1$   $\Gamma$  point-centered Monkhorst-Pack  $k$ -point mesh<sup>71</sup> per  $3 \times 3$  graphene supercell (structure and cell optimization). The electronic density of states (DOS) were calculated using the tetrahedron method with a  $21 \times 21 \times 1$   $k$ -point mesh. For each  $C_x(OH)_yF_z$  ( $x = 3, 4; y = 5, 6$ ) stoichiometry, at least 100 random structures were generated and an extensive study of their structural, electronic, and magnetic properties was

accomplished. Full structural optimization was performed using a quasi-Newton algorithm until the residual atomic forces were lower than  $25 \text{ meV } \text{\AA}^{-1}$ . Simultaneously, the electronic and magnetic degrees of freedom were converged to an energy of less than  $10^{-6} \text{ eV}$ .

By relating the energy difference ( $\Delta E$ ) between the ferromagnetic state and spin singlet with all electrons paired (typically higher in energy by up to several hundreds of meV depending on both the stoichiometry and structural features of G(OH)F system) to the Ising model of the honeycomb lattice, the transition temperature ( $T_c$ ) was estimated.<sup>61,62</sup> The exact solution for the honeycomb lattice resulted in  $k_B T_c / |J| = 0.3797$ , with  $J = \Delta E / 2z$  for  $z$  pairs of spins on radical sites (and  $k_B$  the Boltzmann constant). In the Ising model, one usually relates the magnetic coupling constant ( $J$ ) to the energy difference between the ferromagnetic and antiferromagnetic spin arrangements.<sup>72</sup> We shall note, however, that the G(OH)F system is known to exhibit complex temperature-dependent behavior.<sup>33</sup> Moreover, our calculations converged to the ferromagnetic state and the spin-flip led to solutions with non-zero total magnetic moments, *i.e.*, ferrimagnetic states with spin-flip energy below  $60 \text{ meV}$  (see the Supporting Information for details). Therefore, we modelled the paramagnetic state by a spin singlet with all electrons paired, although the paramagnetic state can be maintained by thermal effects with local moments pointing in random directions. Thus, our approach may provide an upper estimate of  $T_c$ . However, besides inherent difficulties of DFT in describing the dynamic magnetic disorder in the paramagnetic state, such local disorder goes beyond the Ising model and has been shown to provide excellent agreement with the measured magnetic transition temperature.<sup>62</sup>

*Quantum Mechanical Finite Model Calculations.* The initial model structures of partially fluorinated graphene, *i.e.*,  $\text{C}_{18}\text{F}_{10}$ , and  $\text{C}_{18}(\text{OH})_4\text{F}_6$  for the kinetic stability study were extracted from the PW-DFT-PBC, and link hydrogen atoms were added to saturate any dangling bonds. The

structures were re-optimized at the  $\omega$ B97X-D/6-31+G(d) level of theory<sup>73-75</sup> (keeping the boundary carbon atoms frozen) using the Gaussian09 program (Revision D.01).<sup>76</sup> The size of the model structures was chosen based on the local chemical environment criterion, *i.e.*, all carbon atoms in the vicinity of a reaction site were considered. Reaction energies and activation barriers were obtained by geometry optimizations of the local region containing the two carbon atoms at the reaction site as well as the closest neighboring atoms with their substituents but keeping the rest of the structure frozen.

## ASSOCIATED CONTENT

**Supporting Information.** The Supporting Information is available free of charge on the ACS Publications website at DOI:

Scheme showing purification conditions for the preparation of the G(OH)F system, high-resolution O 1s XPS pattern of the G(OH)F sample, Raman spectrum of the G(OH)F system, AFM topology and height profile of the G(OH)F sample, profiles of the hysteresis loops of the G(OH)F system at low applied magnetic fields, additional EPR spectra of the G(OH)F sample, theoretical calculations of the G(OH)F structures, additional STEM measurements and simulations, and content of various selected metals in the synthesized G(OH)F sample determined from the ICP-MS technique (PDF).

## Notes

The authors declare no competing financial interests.

## AUTHOR INFORMATION

### **Corresponding Authors**

\* radek.zboril@upol.cz (Radek Zbořil), michal.otyepka@upol.cz (Michal Otyepka)

### **Author Contributions**

All the authors participated in the writing of the manuscript. All the authors discussed the results. J. Tuček was responsible for the concept development and performed analysis of magnetization measurements. K. Holá performed synthesis and physicochemical characterization of the prepared systems. G. Zoppellaro performed EPR measurements and analysis. P. Błoński performed modelling of magnetic features. R. Langer performed theoretical calculations on defluorination process and formation of zig-zag patterns. M. Medved' performed stability calculations. T. Susi performed STEM and EELS measurements and their analyses. M. Otyepka was responsible for the theoretical concept and interpreted the theoretical data. R. Zbořil was responsible for the concept development, performed the design of experiment, set the strategy of the work and came with the idea presented in the work. All the authors have given approval to the final version of the manuscript.

## ACKNOWLEDGMENTS

The authors acknowledge support from the Ministry of Education, Youth and Sports of the Czech Republic under Project No. LO1305, the support by the Operational Programme Research, Development and Education – European Regional Development Fund, Project No. CZ.02.1.01/0.0/0.0/16\_019/0000754 of the Ministry of Education, Youth and Sports of the Czech Republic, the assistance provided by the Research Infrastructure NanoEnviCz supported by the

Ministry of Education, Youth and Sports of the Czech Republic under Project No. LM2015073, and the support from the Internal Student Grant Agency (IGA) of the Palacký University in Olomouc, Czech Republic (Project No. IGA\_PrF\_2018\_021). P. B. acknowledges Palacký University institutional support. T. S. acknowledges the Austrian Science Fund (FWF) Project P 28322-N36 and the European Research Council (ERC) Grant No. 756277-ATMEN. M. O. acknowledges funding from the ERC Consolidator Grant (H2020) No. 683024.

## REFERENCES

- (1) Novoselov, K. S.; Geim, A. K.; Morozov, S. V.; Jiang, D.; Zhang, Y.; Dubonos, S. V.; Grigorieva, I. V.; Firsov, A. A. Electric Field Effect in Atomically Thin Carbon Films. *Science* **2004**, *306*, 666–669.
- (2) Castro Neto, A. H.; Guinea, F.; Peres, N. M. R.; Novoselov, K. S.; Geim, A. K. The Electronic Properties of Graphene. *Rev. Modern Phys.* **2009**, *81*, 109–162.
- (3) Novoselov, K. S.; Fal'ko, V. I.; Colombo, L.; Gellert, P. R.; Schwab, M. G.; Kim, K. A Roadmap for Graphene. *Nature* **2012**, *490*, 192–200.
- (4) Tapaszto, L.; Dobrik, G.; Lambin, P.; Biro, L. P. Tailoring the Atomic Structure of Graphene Nanoribbons by Scanning Tunnelling Microscope Lithography. *Nat. Nanotechnol.* **2008**, *3*, 397–401.
- (5) Zhu, Y. W.; Murali, S.; Stoller, M. D.; Ganesh, K. J.; Cai, W. W.; Ferreira, P. J.; Pirkle, A.; Wallace, R. M.; Cychosz, K. A.; Thommes, M.; Su, D.; Stach, E. A.; Ruoff, R. S. Carbon-Based Supercapacitors Produced by Activation of Graphene. *Science* **2011**, *332*, 1537–1541.
- (6) Qu, L. T.; Liu, Y.; Baek, J. B.; Dai, L. M. Nitrogen-Doped Graphene as Efficient Metal-Free Electrocatalyst for Oxygen Reduction in Fuel Cells. *ACS Nano* **2010**, *4*, 1321–1326.
- (7) Liu, Z. F.; Liu, Q.; Huang, Y.; Ma, Y. F.; Yin, S. G.; Zhang, X. Y.; Sun, W.; Chen, Y. S. Organic Photovoltaic Devices Based on a Novel Acceptor Material: Graphene. *Adv. Mater.* **2008**, *20*, 3924–3930.
- (8) Min, S. K.; Kim, W. Y.; Cho, Y.; Kim, K. S. Fast DNA Sequencing with a Graphene-Based Nanochannel Device. *Nat. Nanotechnol.* **2011**, *6*, 162–165.

(9) Zhu, C.; Han, T. Y. J.; Duoss, E. B.; Golobic, A. M.; Kuntz, J. D.; Spadaccini, C. M.; Worsley, M. A. Highly Compressible 3D Periodic Graphene Aerogel Microlattices. *Nat. Commun.* **2015**, *6*, 6962.

(10) Han, Y.; Xu, Z.; Gao, C. Ultrathin Graphene Nanofiltration Membrane for Water Purification. *Adv. Funct. Mater.* **2013**, *23*, 3693–3700.

(11) Shin, M. K.; Lee, B.; Kim, S. H.; Lee, J. A.; Spinks, G. M.; Gambhir, S.; Wallace, G. G.; Kozlov, M. E.; Baughman, R. H.; Kim, S. J. Synergistic Toughening of Composite Fibres by Self-Alignment of Reduced Graphene Oxide and Carbon Nanotubes. *Nat. Commun.* **2012**, *3*, 650.

(12) Georgakilas, V.; Otyepka, M.; Bourlinos, A. B.; Chandra, V.; Kim, N.; Kemp, K. C.; Hobza, P.; Zboril, R.; Kim, K. S. Functionalization of Graphene: Covalent and Non-Covalent Approaches, Derivatives and Applications. *Chem. Rev.* **2012**, *112*, 6156–6214.

(13) Dreyer, D. R.; Park, S.; Bielawski, C. W.; Ruoff, R. S. The Chemistry of Graphene Oxide. *Chem. Soc. Rev.* **2010**, *39*, 228–240.

(14) Elias, D. C.; Nair, R. R.; Mohiuddin, T. M. G.; Morozov, S. V.; Blake, P.; Halsall, M. P.; Ferrari, A. C.; Boukhvalov, D. W.; Katsnelson, M. I.; Geim, A. K.; Novoselov, K. S. Control of Graphene's Properties by Reversible Hydrogenation: Evidence for Graphane. *Science* **2009**, *323*, 610–613.

(15) Zboril, R.; Karlicky, F.; Bourlinos, A. B.; Steriotis, T. A.; Stubos, A. K.; Georgakilas, V.; Safarova, K.; Jancik, D.; Trapalis, C.; Otyepka, M. Graphene Fluoride: A Stable Stoichiometric Graphene Derivative and Its Chemical Conversion to Graphene. *Small* **2010**, *6*, 2885–2891.

(16) Nair, R. R.; Ren, W. C.; Jalil, R.; Riaz, I.; Kravets, V. G.; Britnell, L.; Blake, P.; Schedin, F.; Mayorov, A. S.; Yuan, S. J.; Katsnelson, M. I.; Cheng, H. M.; Strupinski, W.; Bulusheva, L. G.; Okotrub, A. V.; Grigorieva, I. V.; Grigorenko, A. N.; Novoselov, K. S.; Geim, A. K. Fluorographene: A Two-Dimensional Counterpart of Teflon. *Small* **2010**, *6*, 2877–2884.

(17) Karlicky, F.; Datta, K. K. R.; Otyepka, M.; Zboril, R. Halogenated Graphenes: Rapidly Growing Family of Graphene Derivatives. *ACS Nano* **2013**, *7*, 6434–6464.

(18) Urbanova, V.; Hola, K.; Bourlinos, A. B.; Cepe, K.; Ambrosi, A.; Loo, A. H.; Pumera, M.; Karlicky, F.; Otyepka, M.; Zboril, R. Thiofluorographene-Hydrophilic Graphene Derivative with Semiconducting and Genosensing properties. *Adv. Mater.* **2015**, *27*, 2305–2310.

(19) Bakandritsos, A.; Pykal, M.; Blonski, P.; Jakubec, P.; Chronopoulos, D. D.; Polakova, K.; Georgakilas, V.; Cepe, K.; Tomanec, O.; Ranc, V.; Bourlinos, A. B.; Zboril, R.; Otyepka, M. Cyanographene and Graphene Acid: Emerging Derivatives Enabling High-Yield and Selective Functionalization of Graphene. *ACS Nano* **2017**, *11*, 2982–2991.

(20) Jankovsky, O.; Novacek, M.; Luxa, J.; Sedmidubsky, D.; Fila, V.; Pumera, M.; Sofer, Z. A New Member of the Graphene Family: Graphene Acid. *Chem. Eur. J.* **2016**, *22*, 17416–17424.

(21) Ghaderi, N.; Peressi, M. First-Principle Study of Hydroxyl Functional Groups on Pristine, Defected Graphene, and Graphene Epoxide. *J. Phys. Chem. C* **2010**, *114*, 21625–21630.

(22) Georgakilas, V.; Perman, J. A.; Tucek, J.; Zboril, R. Broad Family of Carbon Nanoallotropes: Classification, Chemistry, and Applications of Fullerenes, Carbon Dots, Nanotubes, Graphene, Nanodiamonds, and Combined Superstructures. *Chem. Rev.* **2015**, *115*, 4744–4822.

- (23) Yazyev, O. V. Emergence of Magnetism in Graphene Materials and Nanostructures. *Rep. Prog. Phys.* **2010**, *73*, 056501.
- (24) Červenka, J.; Katsnelson, M. I.; Flipse, C. F. J. Room-Temperature Ferromagnetism in Graphite Driven by Two-Dimensional Networks of Point Defects. *Nat. Phys.* **2009**, *5*, 840–844.
- (25) Yazyev, O. V.; Helm, L. Defect-Induced Magnetism in Graphene. *Phys. Rev. B* **2007**, *75*, 125408.
- (26) Tucek, J.; Blonski, P.; Sofer, Z.; Simek, P.; Petr, M.; Pumera, M.; Otyepka, M.; Zboril, R. Sulfur Doping Induces Strong Ferromagnetic Ordering in Graphene: Effect of Concentration and Substitution Mechanism. *Adv. Mater.* **2016**, *28*, 5045–5053.
- (27) Blonski, P.; Tucek, J.; Sofer, Z.; Mazanek, V.; Petr, M.; Pumera, M.; Otyepka, M.; Zboril, R. Doping with Graphitic Nitrogen Triggers Ferromagnetism in Graphene. *J. Am. Chem. Soc.* **2017**, *139*, 3171–3180.
- (28) Zhou, J.; Wang, Q.; Sun, Q.; Chen, X. S.; Kawazoe, Y.; Jena, P. Ferromagnetism in Semihydrogenated Graphene Sheet. *Nano Lett.* **2009**, *9*, 3867–3870.
- (29) Nair, R. R.; Sepioni, M.; Tsai, I. L.; Lehtinen, O.; Keinonen, J.; Krasheninnikov, A. V.; Thomson, T.; Geim, A. K.; Grigorieva, I. V. Spin-Half Paramagnetism in Graphene Induced by Point Defects *Nat. Phys.* **2012**, *8*, 199–202.
- (30) Eng, A. Y. S.; Poh, H. L.; Sanek, F.; Marysko, M.; Matejkova, S.; Sofer, Z.; Pumera, M. Searching for Magnetism in Hydrogenated Graphene: Using Highly Hydrogenated Graphene Prepared *via* Birch Reduction of Graphite Oxides. *ACS Nano* **2013**, *7*, 5930–5939.

- (31) Eng, A. Y. S.; Sofer, Z.; Huber, S.; Bousa, D.; Marysko, M.; Pumera, M. Hydrogenated Graphenes by Birch Reduction: Influence of Electron and Proton Sources on Hydrogenation Efficiency, Magnetism, and Electrochemistry. *Chem. Eur. J.* **2015**, *21*, 16828–16838.
- (32) Gonzalez-Herrero, H.; Gomez-Rodriguez, J. M.; Mallet, P.; Moaied, M.; Palacios, J. J.; Salgado, C.; Ugeda, M. M.; Veuillen, J. Y.; Yndurain, F.; Brihuega, I. Atomic-Scale Control of Graphene Magnetism by Using Hydrogen Atoms. *Science* **2016**, *352*, 437–441.
- (33) Tucek, J.; Hola, K.; Bourlinos, A. B.; Blonski, P.; Bakandritsos, A.; Ugolotti, J.; Dubecky, M.; Karlicky, F.; Ranc, V.; Cepe, K.; Otyepka, M.; Zboril, R. Room Temperature Organic Magnets Derived from  $sp^3$  Functionalized Graphene. *Nat. Commun.* **2017**, *8*, 14525.
- (34) Boukhvalov, D. W.; Katsnelson, M. I.  $sp$  Electron Magnetic Clusters with a Large Spin in Graphene. *ACS Nano* **2011**, *5*, 2440–2446.
- (35) Kobayashi, Y.; Fukui, K.; Enoki, T.; Kusakabe, K.; Kaburagi, Y. Observation of Zigzag and Armchair Edges of Graphite Using Scanning Tunneling Microscopy and Spectroscopy. *Phys. Rev. B* **2005**, *71*, 193406.
- (36) Magda, G. Z.; Jin, X. Z.; Hagymasi, I.; Vancso, P.; Osvath, Z.; Nemes-Incze, P.; Hwang, C. Y.; Biro, L. P.; Tapasztó, L. Room-Temperature Magnetic Order on Zigzag Edges of Narrow Graphene Nanoribbons. *Nature* **2014**, *514*, 608–611.
- (37) Lieb, E. H. 2 Theorems on the Hubbard Model. *Phys. Rev. Lett.* **1989**, *62*, 1201–1204.
- (38) Hong, J.; Bekyarova, E.; de Heer, W. A.; Haddon, R. C.; Khizroev, S. Chemically Engineered Graphene-Based 2D Organic Molecular Magnet. *ACS Nano* **2013**, *7*, 10011–10022.

(39) Makarova, T. L.; Sundqvist, B.; Hohne, R.; Esquinazi, P.; Kopelevich, Y.; Scharff, P.; Davydov, V. A.; Kashevarova, L. S.; Rakhmanina, A. V. Magnetic Carbon. *Nature* **2001**, *413*, 716–718.

(40) Makarova, T. L.; Sundqvist, B.; Hohne, R.; Esquinazi, P.; Kopelevich, Y.; Scharff, P.; Davydov, V. A.; Kashevarova, L. S.; Rakhmanina, A. V. Retraction: Magnetic Carbon. *Nature* **2006**, *440*, 707.

(41) Tang, T.; Tang, N. J.; Zheng, Y. P.; Wan, X. G.; Liu, Y.; Liu, F. C.; Xu, Q. H.; Du, Y. W. Robust Magnetic Moments on the Basal Plane of the Graphene Sheet Effectively Induced by OH Groups. *Sci. Rep.* **2015**, *5*, 8448.

(42) Tucek, J.; Blonski, P.; Ugolotti, J.; Swain, A. K.; Enoki, T.; Zboril, R. Emerging Chemical Strategies for Imprinting Magnetism in Graphene and Related 2D Materials for Spintronic and Biomedical Applications. *Chem. Soc. Rev.* **2018**, *47*, 3899–3990.

(43) Pumera, M.; Sofer, Z. Towards Stoichiometric Analogues of Graphene: Graphane, Fluorographene, Graphol, Graphene Acid and Others. *Chem. Soc. Rev.* **2017**, *46*, 4450–4463.

(44) Sturala, J.; Luxa, J.; Pumera, M.; Sofer, Z. Chemistry of Graphene Derivatives: Synthesis, Applications, and Perspectives. *Chem. Eur. J.* **2018**, *24*, 5992–6006.

(45) Chronopoulos, D. D.; Bakandritsos, A.; Pykal, M.; Zboril, R.; Otyepka, M. Chemistry, Properties, and Applications of Fluorographene. *Appl. Mater. Today* **2017**, *9*, 60–70.

(46) Petit, P.; Joguet, E.; Fischer, J. E.; Rinzler, A. G.; Smalley, R. E. Electron Spin Resonance and Microwave Resistivity of Single-Wall Carbon Nanotubes. *Phys. Rev. B* **1997**, *56*, 9275–9278.

- (47) Likodimos, V.; Glenis, S.; Guskos, N.; Lin, C. L. Antiferromagnetic Behavior in Single-Wall Carbon Nanotubes. *Phys. Rev. B* **2007**, *76*, 075420.
- (48) Rao, S. S.; Stesmans, A.; Noyen, J. V.; Jacobs, P.; Sels, B. Electron Spin Resonance Investigation of Ultra-Small Double Walled Carbon Nanotubes Embedded in Zeolite Nanochannels. *J. Phys. Condens. Matter* **2011**, *23*, 455801.
- (49) van Vleck, J. H. The Dipolar Broadening of Magnetic Resonance Lines in Crystals. *Phys. Rev.* **1948**, *74*, 1168–1183.
- (50) Anderson, P. W.; Weiss, P. R. Exchange Narrowing in Paramagnetic Resonance. *Mod. Phys.* **1953**, *25*, 269–276.
- (51) Kubo, R.; Tomita, K. A General Theory of Magnetic Resonance Absorption. *J. Phys. Soc. Jpn.* **1954**, *9*, 888–919.
- (52) Anderson, P. W. A Mathematical Model for the Narrowing of Spectral Lines by Exchange or Motion. *J. Phys. Soc. Jpn.* **1954**, *9*, 316–319.
- (53) Panich, M.; Shames, A. I.; Nakajima, T. On Paramagnetism in Fluorinated Graphite: EPR and Solid State NMR Study. *J. Phys. Chem. Sol.* **2001**, *62*, 959–964.
- (54) Castner, T. G. Saturation of the Paramagnetic Resonance of a V Center. *Phys. Rev.* **1959**, *115*, 1506–1515.
- (55) Portis, A. M. Electronic Structure of F-Centers – Saturation of the Electron Spin Resonance. *Phys. Rev.* **1953**, *91*, 1071–1078.

- (56) Zoppellaro, G.; Geies, A.; Andersson, K. K.; Enkelmann, V.; Baumgarten, M. Synthesis, Optical Properties and Magnetic Studies of 2,6-bis(pyrazolylmethyl)pyridine Functionalized with Two Nitronyl Nitroxide Radicals. *Eur. J. Org. Chem.* **2008**, 1431–1440.
- (57) Kosaka, M.; Ebbesen, T. W.; Hiura, H.; Tanigaki, K. Electron Spin Resonance of Carbon Nanotubes. *Chem. Phys. Lett.* **1994**, 225, 161–164.
- (58) Shibayama, Y.; Sato, H.; Enoki, T.; Endo, M. Disordered Magnetism at the Metal-Insulator Threshold in Nano-Graphite-Based Carbon Materials. *Phys. Rev. Lett.* **2000**, 84, 1744–1747.
- (59) Lee, K. W.; Lee, C. E. Electron Spin Resonance of Proton-Irradiated Graphite. *Phys. Rev. Lett.* **2006**, 97, 137206.
- (60) Wang, B.; Wang, J. J.; Zhu, J. Fluorination of Graphene: A Spectroscopic and Microscopic Study. *ACS Nano* **2014**, 8, 1862–1870.
- (61) Balcerzak, T.; Szalowski, K.; Jascur, M.; Zukovic, M.; Bobak, A.; Borovsky, M. Thermodynamic Description of the Ising Antiferromagnet on a Triangular Lattice with Selective Dilution by a Modified Pair-Approximation Method. *Phys. Rev. E* **2014**, 89, 062140.
- (62) Tuček, J.; Błoński, P.; Malina, O.; Pumera, M.; Chua, C. K.; Otyepka, M.; Zbořil, R. Morphology-Dependent Magnetism in Nanographene: Beyond Nanoribbons. *Adv. Funct. Mater.* **2018**, 28, 1800592.
- (63) Susi, T.; Hardcastle, T. P.; Hofsass, H.; Mittelberger, A.; Pennycook, T. J.; Mangler, C.; Drummond-Brydson, R.; Scott, A. J.; Meyer, J. C.; Kotakoski, J. Single-Atom Spectroscopy of Phosphorus Dopants Implanted into Graphene. *2D Mater.* **2017**, 4, 021013.

- (64) Susi, T.; Madsen, J.; Ludacka, U.; Mortensen, J. J.; Pennycook, T. J.; Lee, Z.; Kotakoski, J.; Kaiser, U.; Meyer, J. C. Efficient First Principles Simulation of Electron Scattering Factors for Transmission Electron Microscopy. *Ultramicroscopy* **2019**, *197*, 16–22.
- (65) Koch, C. *Determination of Core Structure Periodicity and Point Defect Density along Dislocations*. Ph.D. Thesis, Arizona State University, **2002**.
- (66). Rez, D.; Rez, P.; Grant, I. Dirac-Fock Calculations of X-ray Scattering Factors and Contributions to the Mean Inner Potential for Electron Scattering. *Acta Cryst. A* **1994**, *50*, 481–497.
- (67) Kresse, G.; Furthmüller, J. Efficient Iterative Schemes For *Ab Initio* Total-Energy Calculations Using a Plane-Wave Basis Set. *Phys. Rev. B* **1996**, *54*, 11169–11186.
- (68) Perdew, J. P.; Burke, K.; Ernzerhof, M. Generalized Gradient Approximation Made Simple. *Phys. Rev. Lett.* **1996**, *77*, 3865–3868.
- (69) Blöchl, P. E. Projector Augmented-Wave Method. *Phys. Rev. B* **1994**, *50*, 17953–17979.
- (70) Kresse, G.; Joubert, D. From Ultrasoft Pseudopotentials to the Projector Augmented-Wave Method. *Phys. Rev. B* **1999**, *59*, 1758–1775.
- (71) Monkhorst, H. J.; Pack, J. D. Special Points for Brillouin-Zone Integrations. *Phys. Rev. B* **1976**, *13*, 5188–5192.
- (72) Moreira, I. P. R.; Illas, F. *Ab Initio* Theoretical Comparative Study of Magnetic Coupling in  $\text{KNiF}_3$  and  $\text{K}_2\text{NiF}_4$ . *Phys. Rev. B* **1997**, *55*, 4129–4137.

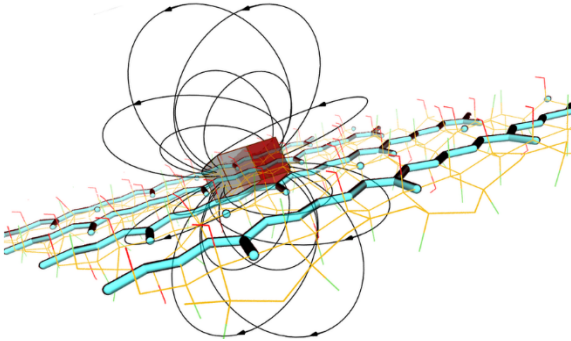
(73) Chai, J.-D.; Head-Gordon, M. Long-Range Corrected Hybrid Density Functionals with Damped Atom-Atom Dispersion Corrections. *Phys. Chem. Chem. Phys.* **2008**, *10*, 6615–6620.

(74) Hehre, W. J.; Ditchfield, R.; Pople, J. A. Self-Consistent Molecular Orbital Methods. XII. Further Extensions of Gaussian-Type Basis Sets for Use in Molecular-Orbital Studies of Organic-Molecules. *J. Chem. Phys.* **1972**, *56*, 2257–2261.

(75) Clark, T.; Chandrasekhar, J.; Spitznagel, G. W.; Schleyer, P. V. R. Efficient Diffuse Function-Augmented Basis-Sets for Anion Calculations. 3. The 3-21+G Basis Set for 1<sup>st</sup> Row Elements, Li-F. *J. Comp. Chem.* **1983**, *4*, 294–301.

(76) Frisch, M. J.; Trucks, G. W.; Schlegel, H. B.; Scuseria, G. E.; Robb, M. A.; Cheeseman, J. R.; Scalmani, G.; Barone, V.; Petersson, G. A.; Nakatsuji, H.; Li, X.; Caricato, M.; Marenich, A.; Bloino, J.; Janesko, B. G.; Gomperts, R.; Mennucci, B.; Hratchian, H. P.; Ortiz, J. V.; Izmaylov, A. F.; Sonnenberg, J. L.; Williams-Young, D.; Ding, F.; Lipparini, F.; Egidi, F.; Goings, J.; Peng, B.; Petrone, A.; Henderson, T.; Ranasinghe, D.; Zakrzewski, V. G.; Gao, J.; Rega, N.; Zheng, G.; Liang, W.; Hada, M.; Ehara, M.; Toyota, K.; Fukuda, R.; Hasegawa, J.; Ishida, M.; Nakajima, T.; Honda, Y.; Kitao, O.; Nakai, H.; Vreven, T.; Throssell, K.; Montgomery, Jr., J. A.; Peralta, J. E.; Ogliaro, F.; Bearpark, M.; Heyd, J. J.; Brothers, E.; Kudin, K. N.; Staroverov, V. N.; Keith, T.; Kobayashi, R.; Normand, J.; Raghavachari, K.; Rendell, A.; Burant, J. C.; Iyengar, S. S.; Tomasi, J.; Cossi, M.; Millam, J. M.; Klene, M.; Adamo, C.; Cammi, R.; Ochterski, J. W.; Martin, R. L.; Morokuma, K.; Farkas, O.; Foresman, J. B.; Fox, D. J. *Gaussian 09, Revision D.01*, Gaussian, Inc., Wallingford CT, **2016**.

TABLE OF CONTENT (TOC) GRAPHICS



# Supporting Information

for

## **Zigzag $sp^2$ Carbon Chains Passing through an $sp^3$ Framework: A Driving Force toward Room-Temperature Ferromagnetic Graphene**

*Jiří Tuček,<sup>1</sup> Kateřina Holá,<sup>1</sup> Giorgio Zoppellaro,<sup>1</sup> Piotr Błoński,<sup>1</sup> Rostislav Langer,<sup>1</sup> Miroslav Medved',<sup>1</sup> Toma Susi,<sup>2</sup> Michal Otyepka,<sup>1,\*</sup> and Radek Zbořil<sup>1,\*</sup>*

<sup>1</sup> Regional Centre of Advanced Technologies and Materials, Department of Physical Chemistry, Faculty of Science, Palacký University in Olomouc, Šlechtitelů 27, 783 71 Olomouc, Czech Republic.

<sup>2</sup> University of Vienna, Faculty of Physics, Boltzmanngasse 5, 1090 Vienna, Austria.

\* Corresponding authors: Phone: +420 585634337, Fax: +420 585634761, E-mail address: radek.zboril@upol.cz (Radek Zbořil); Phone: +420 585634764, Fax: +420 585634761, E-mail address: michal.otyepka@upol.cz (Michal Otyepka).

Number of Figures: 30

Number of Tables: 1

Number of Supporting Information References: 6

Number of Pages: 31

## Supporting Figures

### Purification and selection of the oxygen rich fraction

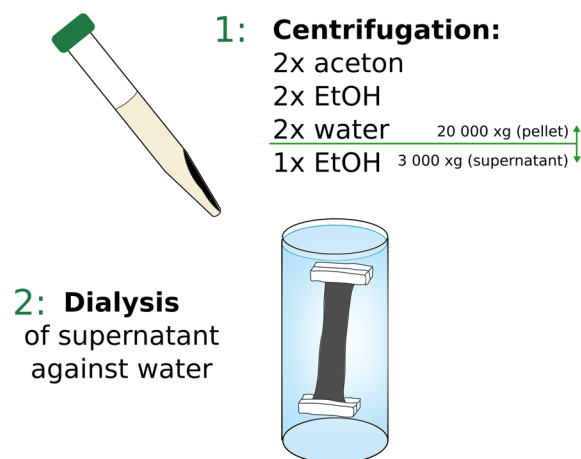


**Figure S1.** Scheme showing purification conditions for the preparation of hydroxofluorographene (G(OH)F) system.

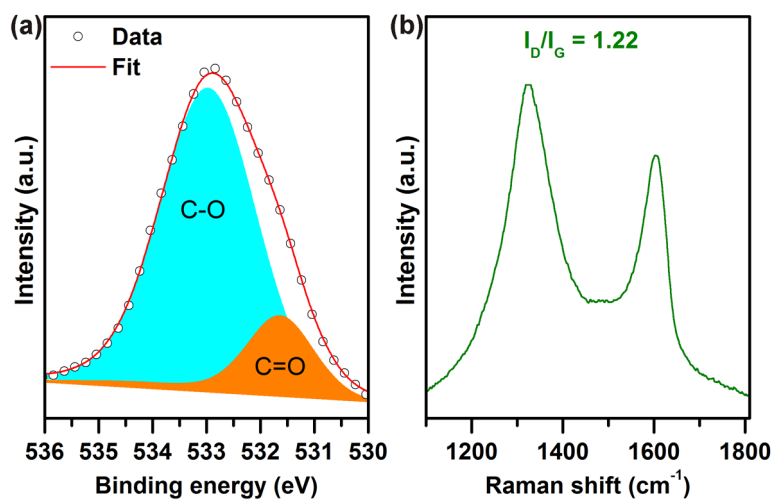


**Figure S2.** Physicochemical characterization of the prepared G(OH)F system. (a) High-resolution O 1s XPS pattern of G(OH)F with identified bonds indicated. (b) Raman spectrum of G(OH)F with the intensity ratio of the D- and G-band indicated.

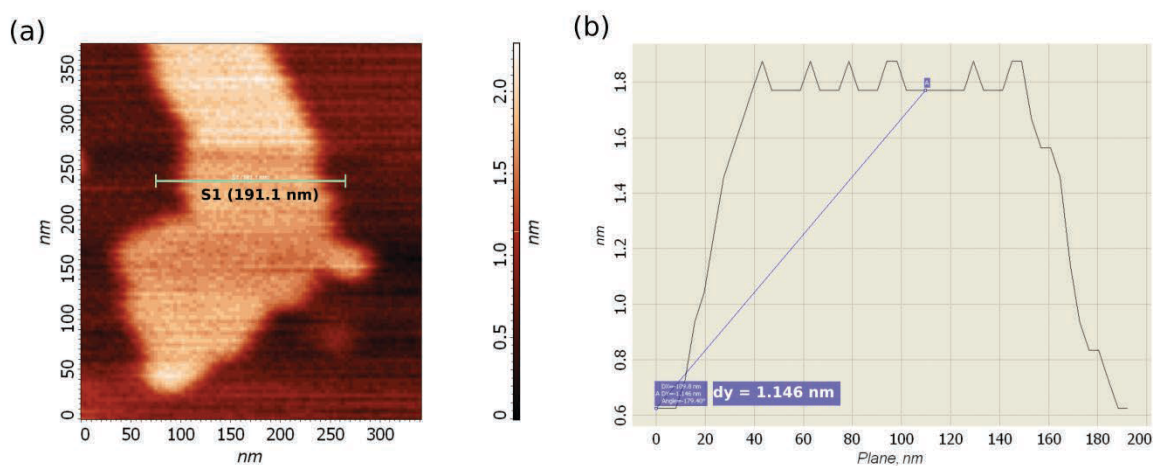


**Figure S3.** (a) Atomic force microscopy (AFM) topology and (b) AFM height profile of the G(OH)F system.

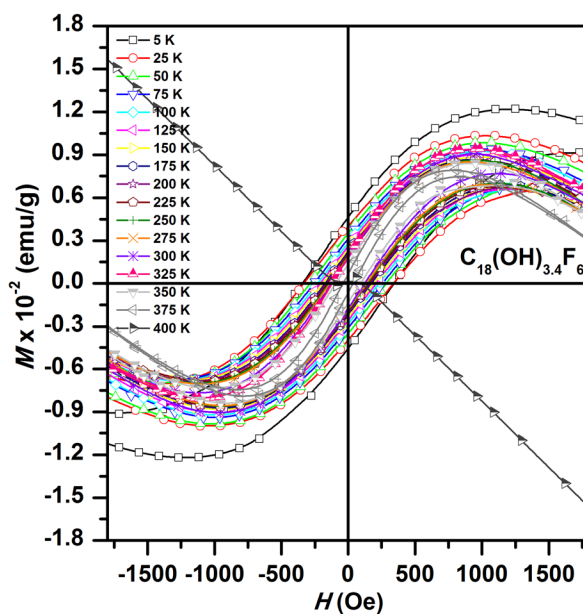


**Figure S4.** Magnetization measurements of the G(OH)F system. Profiles of the hysteresis loops of the G(OH)F sample at low applied magnetic fields, measured at various temperatures between 5 to 400 K, with a clear evolution of the coercivity and remanent magnetization with the temperature.

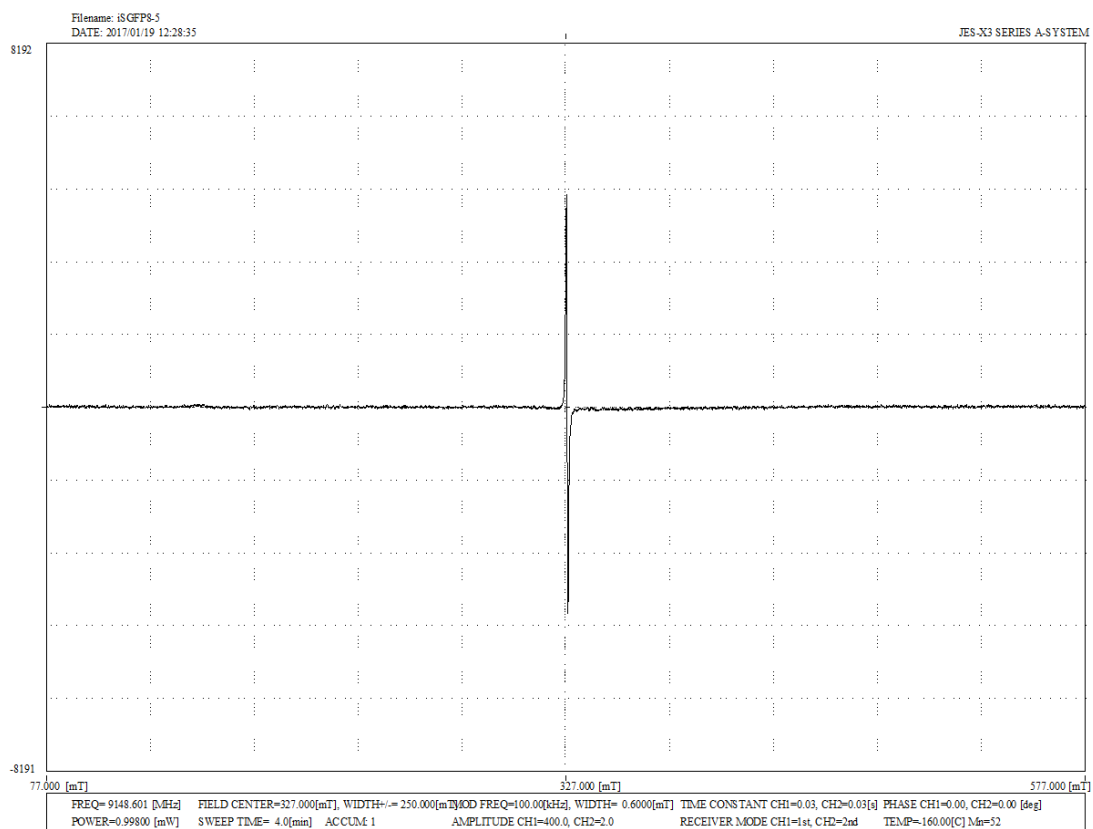


**Figure S5.** X-band EPR spectrum of the G(OH)F system recorded at  $T = 113$  K. Experimental parameters are given in the bottom of the spectrum plot.

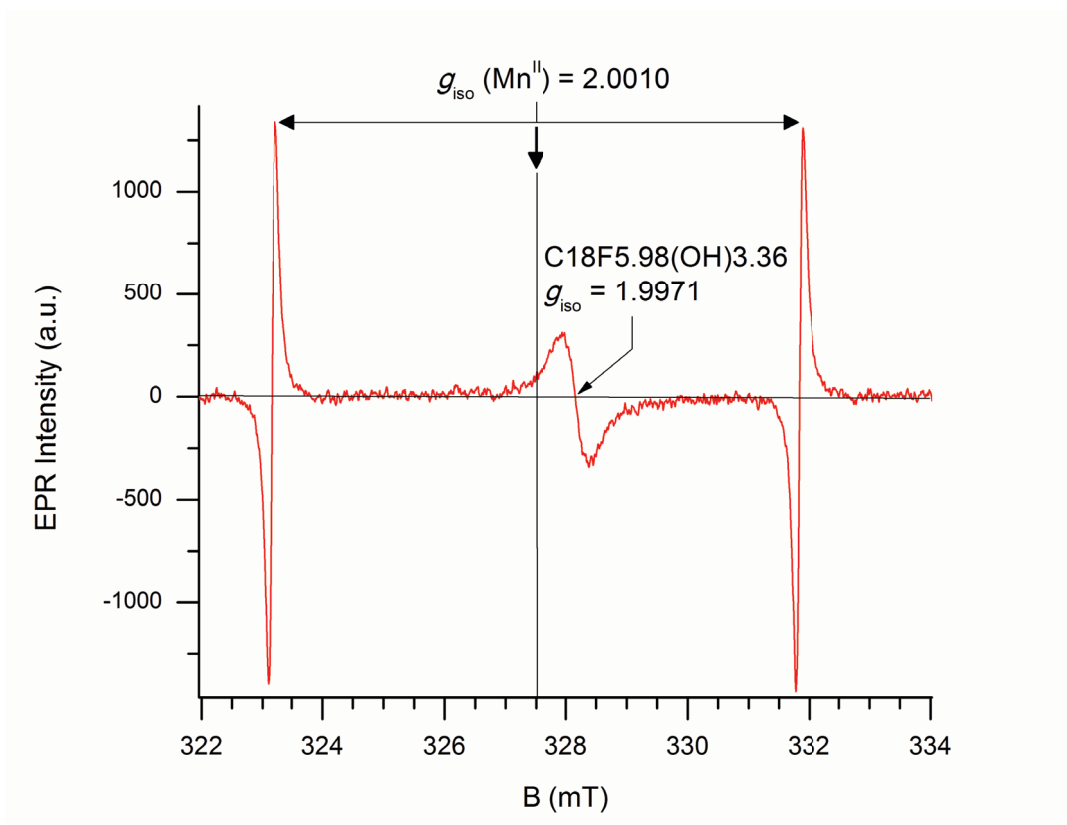


**Figure S6.** Determination of  $g_{\text{eff}}$ -value of the G(OH)F system using the  $\text{Mn}^{\text{II}}\text{MgO}$  standard ( $g_{\text{st}} = 2.00101 \pm 0.00005$ ) at  $T = 113$  K in the enlarged region between the 3<sup>rd</sup> and 4<sup>th</sup> Mn(II) line.

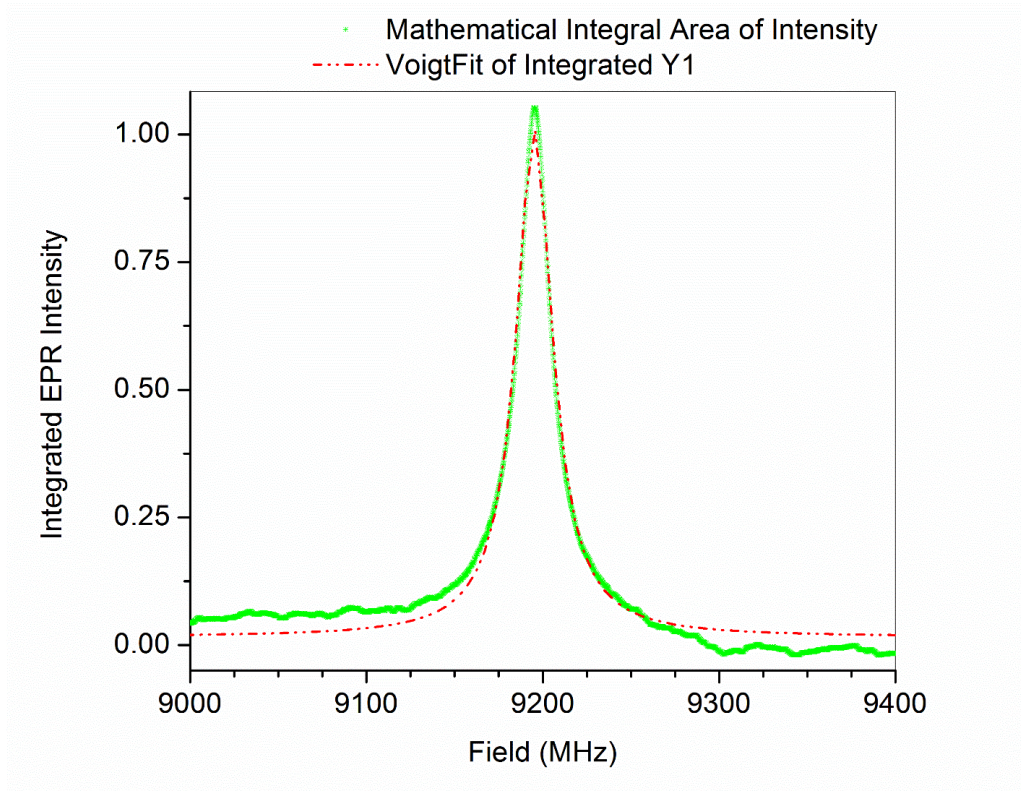


**Figure S7.** The integrated X-band EPR spectrum of the G(OH)F system recorded at  $T = 113$  K. Experimental conditions: 9.170045 GHz frequency, 100 KHz modulation frequency, 0.03 s time constant, 0.1 mW microwave power, 0.2 mT modulation width, 4 min sweep time. The red line corresponds to the resonance signal fitting using the Voigt function (see the table below), *i.e.*,

$$y = y_0 + A \frac{2 \ln 2}{\pi^{3/2}} \frac{W_L}{W_G^2} \int_{-\infty}^{\infty} \frac{e^{-t^2}}{\left(\sqrt{\ln 2} \frac{W_L}{W_G}\right)^2 + \left(\sqrt{4 \ln 2} \frac{x-x_c}{W_G} - t\right)^2} dt$$

Adj. R-Square	0.97462	
		Value
Integrated Y1	$y_0$	9.48023
Integrated Y1	$x_c$	328.08256
Integrated Y1	$A$	844.75122
Integrated Y1	$w_G$	$2.33808 \times 10^{-5}$
Integrated Y1	$w_L$	0.90168

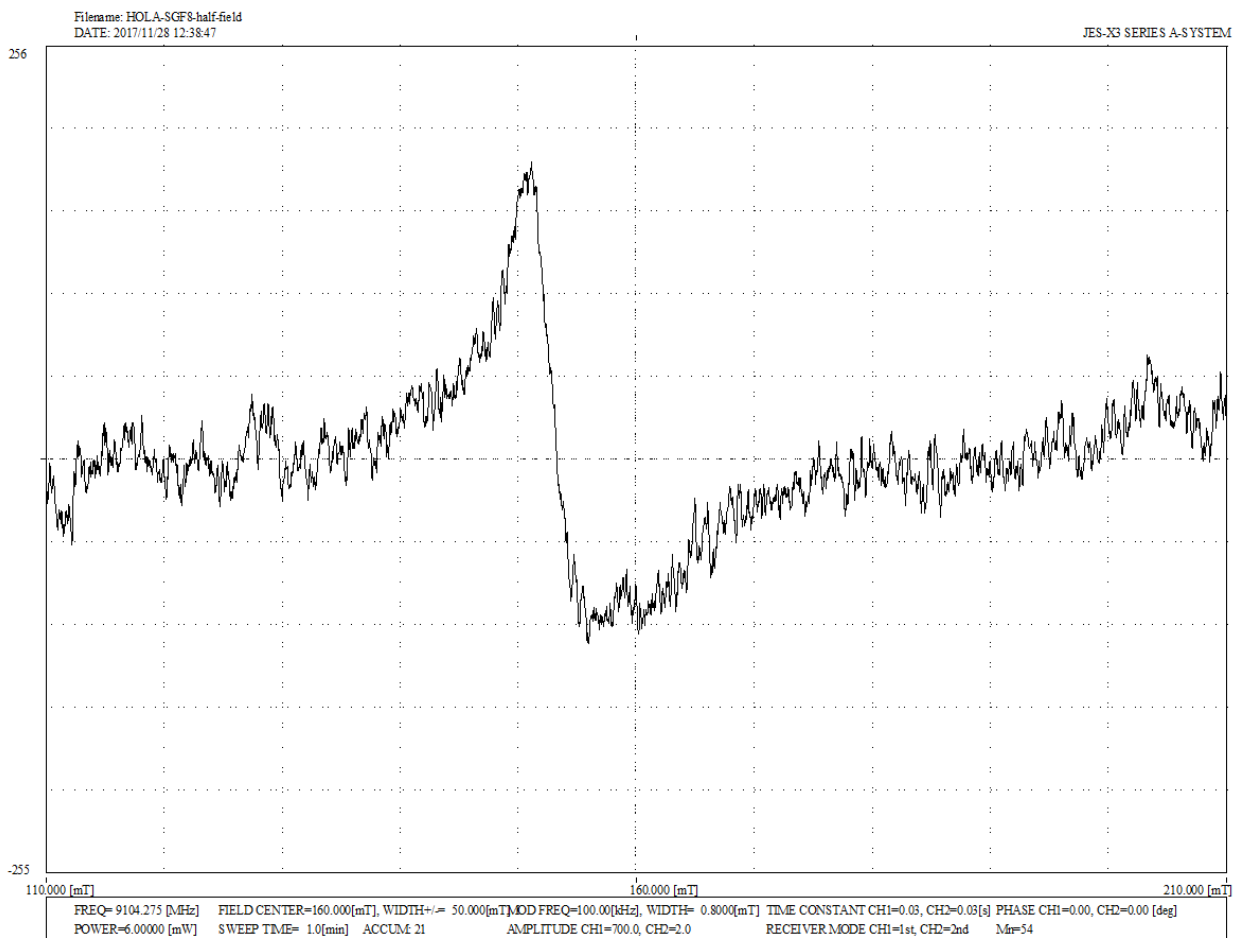


**Figure S8.** X-band EPR spectrum of the G(OH)F system recorded at  $T = 77$  K showing the emergence of the half-field transition (around  $g \approx 4.00$ ). Experimental parameters are given in the bottom of the spectrum plot.

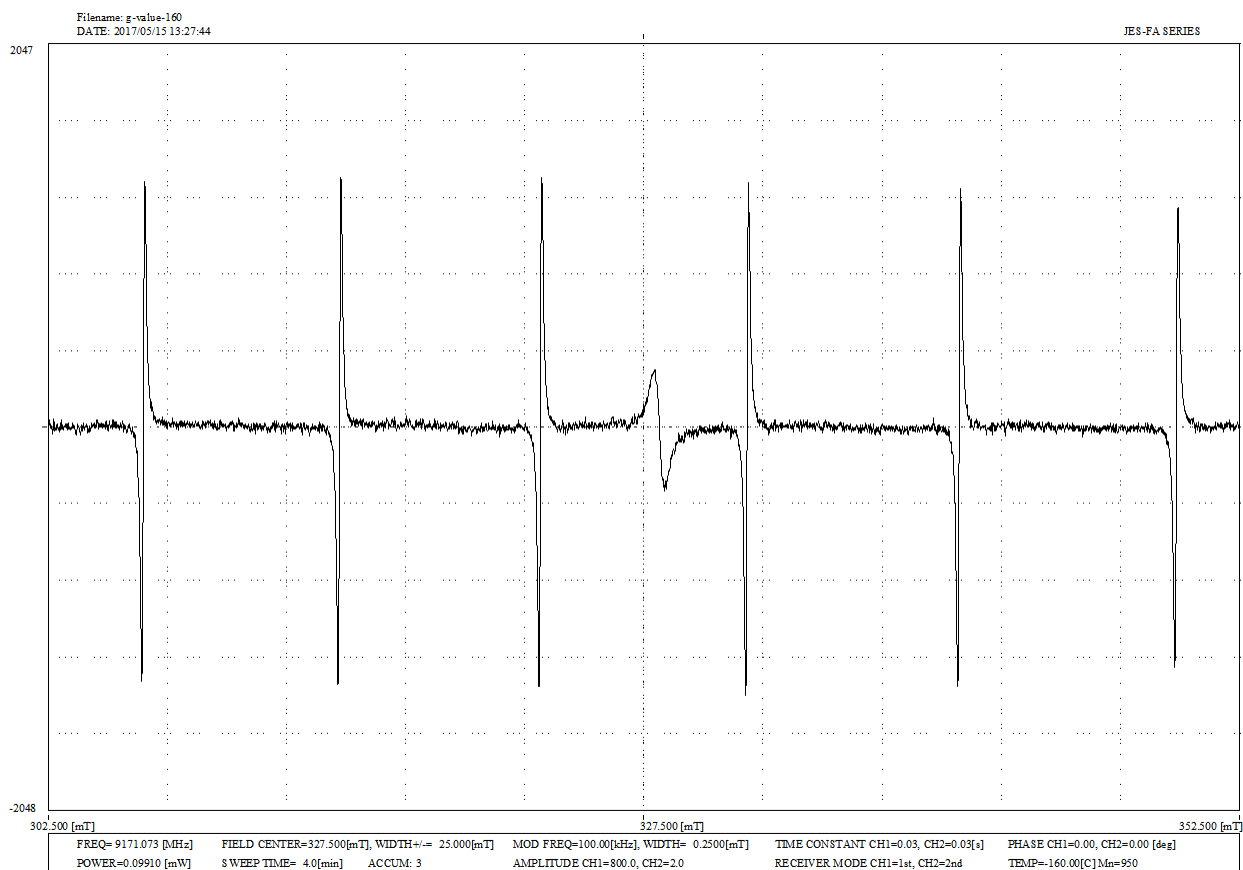


**Figure S9.** Determination of  $g_{\text{eff}}$ -value of the G(OH)F system using the  $\text{Mn}^{\text{II}}\text{MgO}$  standard ( $g_{\text{st}} = 2.00101 \pm 0.00005$ ) at  $T = 113$  K. Experimental acquisition parameters are given in the spectrum plot.

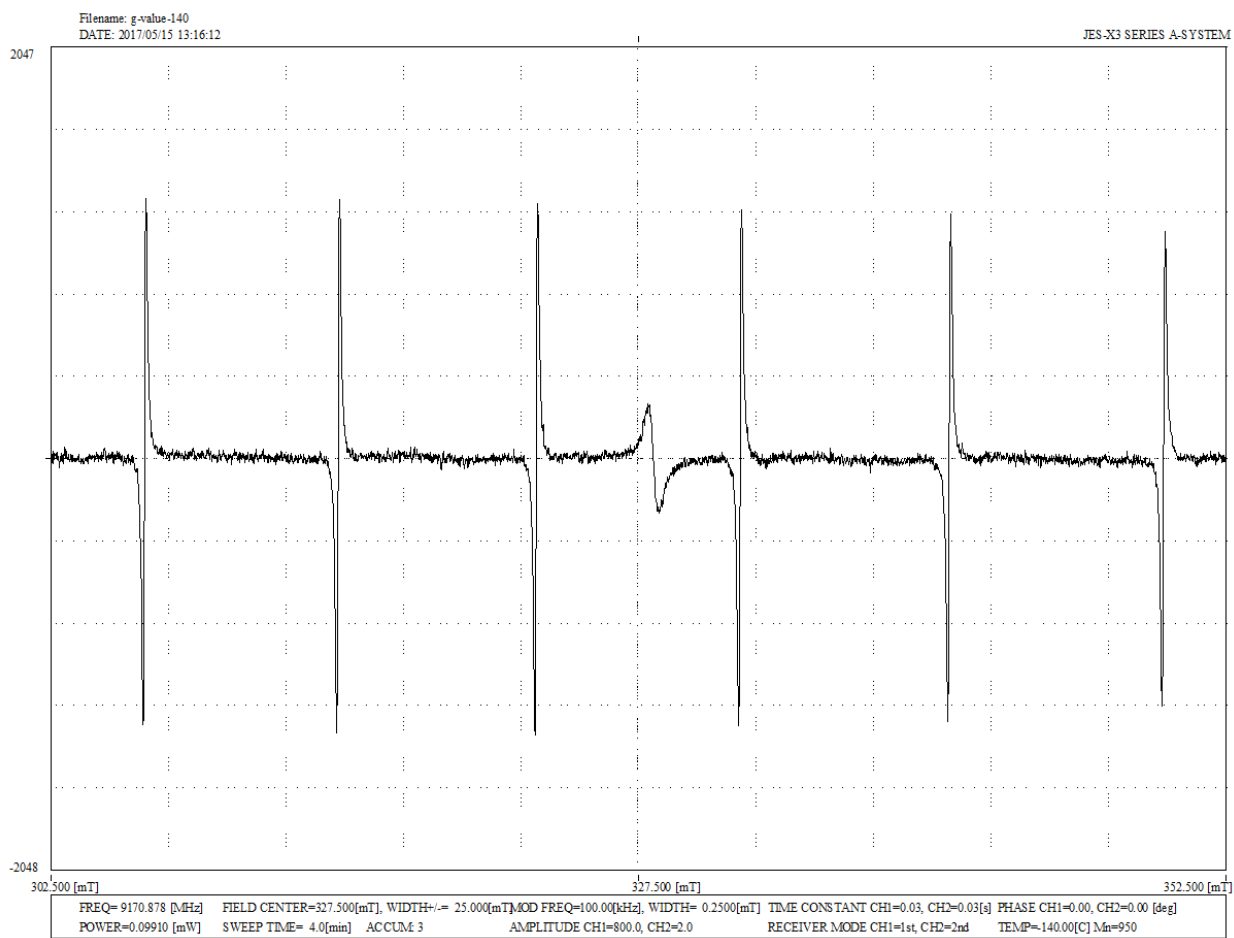


**Figure S10.** Determination of  $g_{\text{eff}}$ -value of the G(OH)F system using the  $\text{Mn}^{\text{II}}\text{MgO}$  standard ( $g_{\text{st}} = 2.00101 \pm 0.00005$ ) at  $T = 133$  K. Experimental acquisition parameters are given in the spectrum plot.

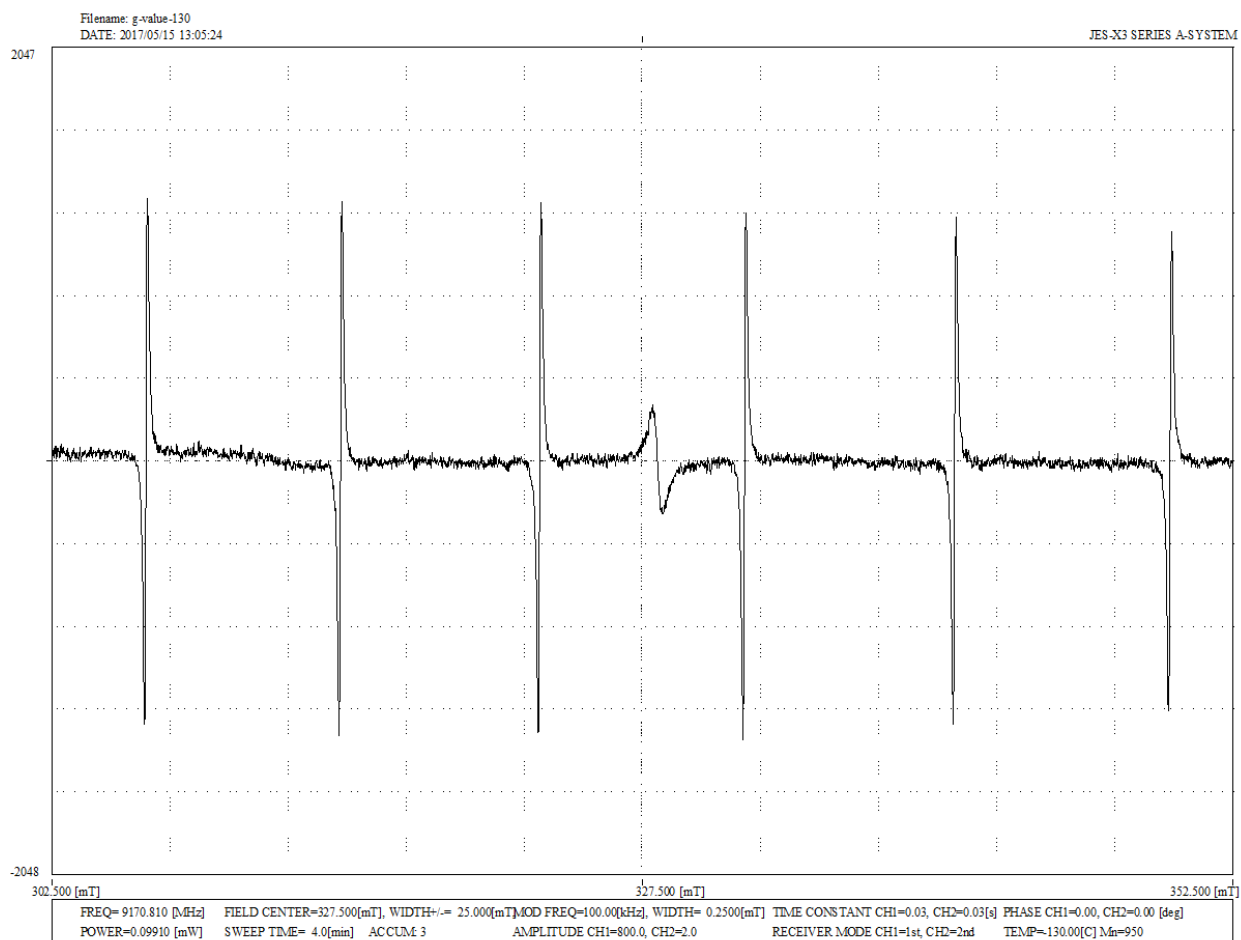


**Figure S11.** Determination of  $g_{\text{eff}}$ -value of the G(OH)F system using the  $\text{Mn}^{\text{II}}\text{MgO}$  standard ( $g_{\text{st}} = 2.00101 \pm 0.00005$ ) at  $T = 143$  K. Experimental acquisition parameters are given in the spectrum plot.

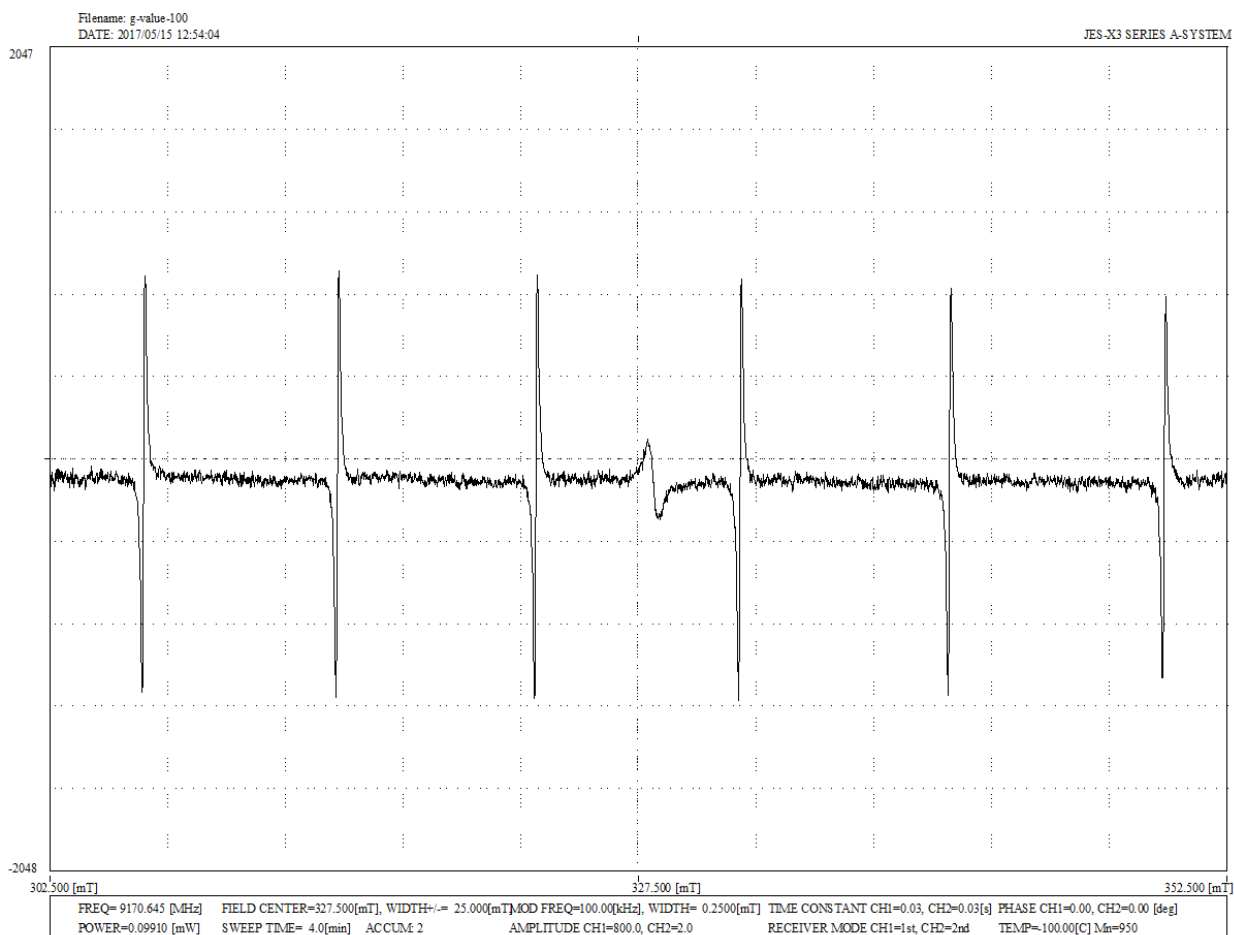


**Figure S12.** Determination of  $g_{\text{eff}}$ -value of the G(OH)F system using the  $\text{Mn}^{\text{II}}\text{MgO}$  standard ( $g_{\text{st}} = 2.00101 \pm 0.00005$ ) at  $T = 173$  K. Experimental acquisition parameters are given in the spectrum plot.

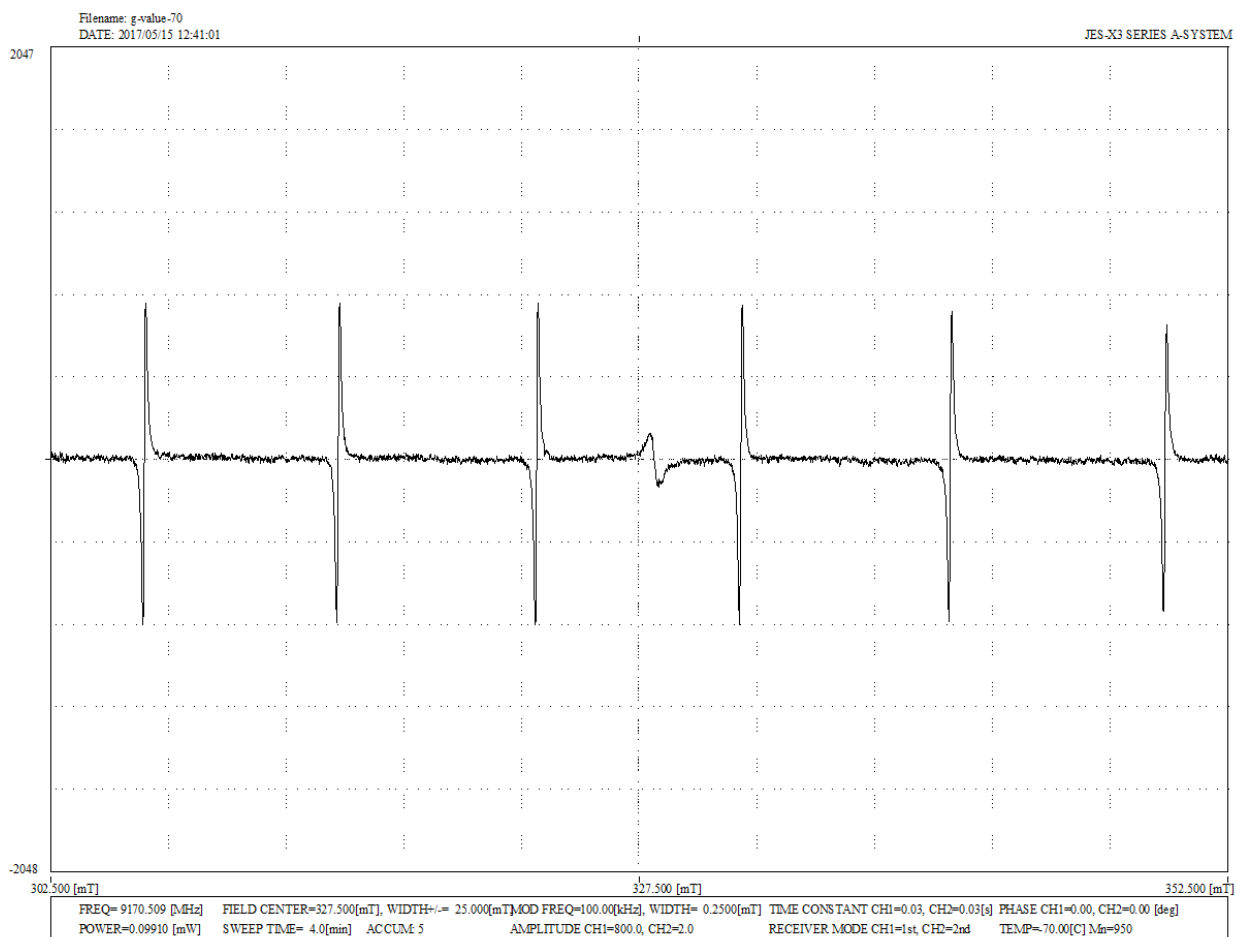


**Figure S13.** Determination of  $g_{\text{eff}}$ -value of the G(OH)F system using the  $\text{Mn}^{\text{II}}\text{MgO}$  standard ( $g_{\text{st}} = 2.00101 \pm 0.00005$ ) at  $T = 203$  K. Experimental acquisition parameters are given in the spectrum plot.

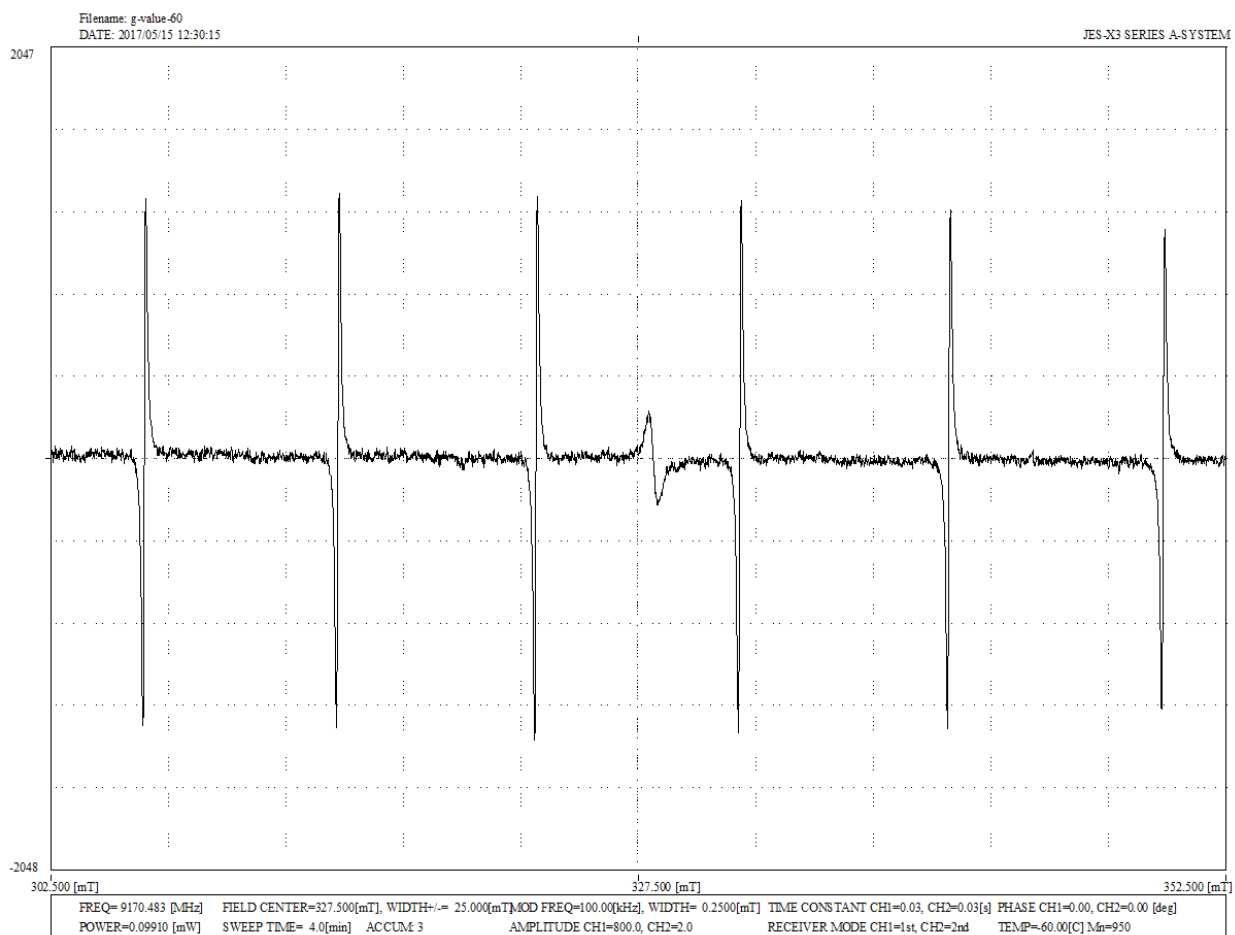


**Figure S14.** Determination of  $g_{\text{eff}}$ -value of the G(OH)F system using the  $\text{Mn}^{\text{II}}\text{MgO}$  standard ( $g_{\text{st}} = 2.00101 \pm 0.00005$ ) at  $T = 213$  K. Experimental acquisition parameters are given in the spectrum plot.

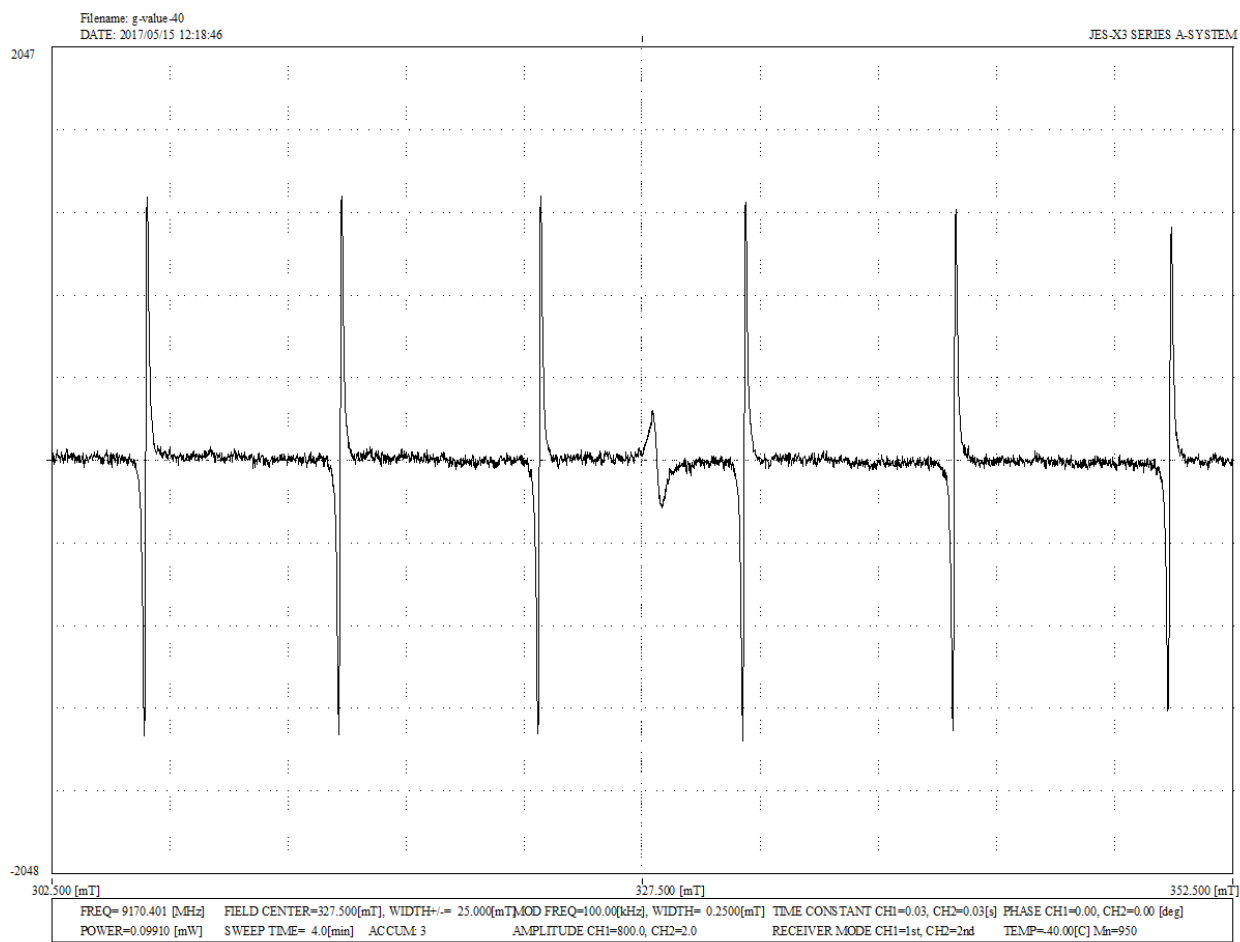


**Figure S15.** Determination of  $g_{\text{eff}}$ -value of the G(OH)F system using the  $\text{Mn}^{\text{II}}\text{MgO}$  standard ( $g_{\text{st}} = 2.00101 \pm 0.00005$ ) at  $T = 233$  K. Experimental acquisition parameters are given in the spectrum plot.

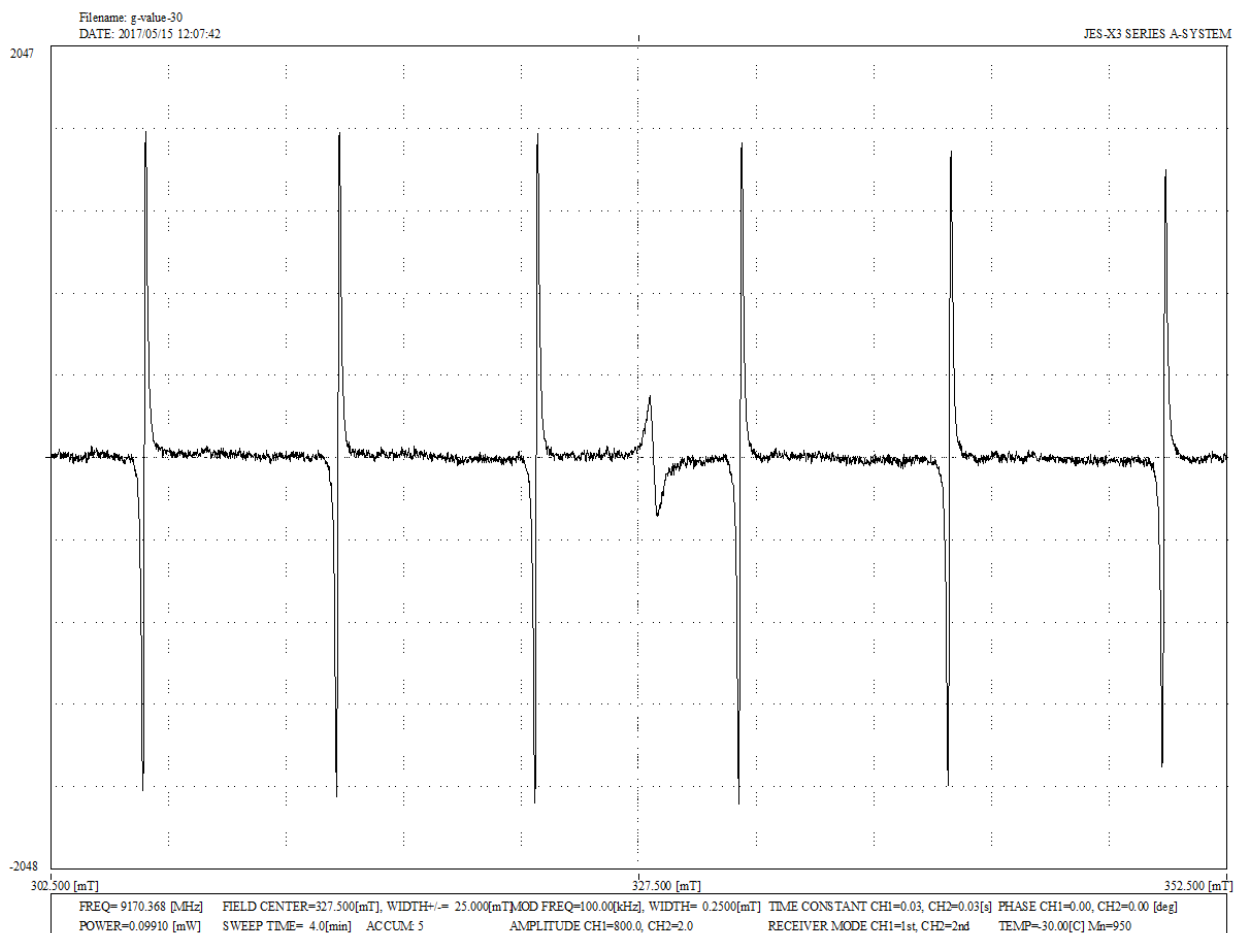


**Figure S16.** Determination of  $g_{\text{eff}}$ -value of the G(OH)F system using the  $\text{Mn}^{\text{II}}\text{MgO}$  standard ( $g_{\text{st}} = 2.00101 \pm 0.00005$ ) at  $T = 243$  K. Experimental acquisition parameters are given in the spectrum plot.

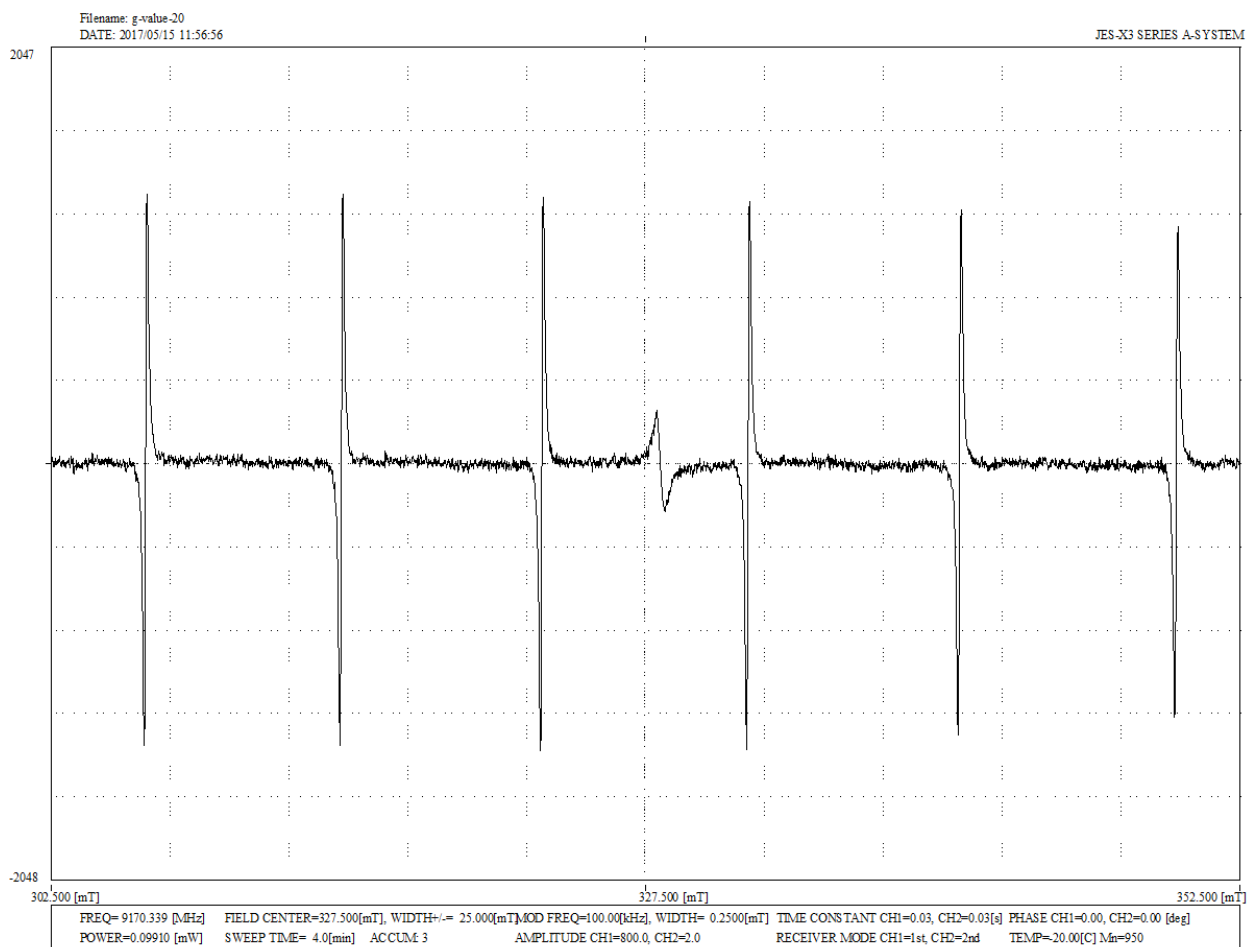


**Figure S17.** Determination of  $g_{\text{eff}}$ -value of the G(OH)F system using the  $\text{Mn}^{\text{II}}\text{MgO}$  standard ( $g_{\text{st}} = 2.00101 \pm 0.00005$ ) at  $T = 253$  K. Experimental acquisition parameters are given in the spectrum plot.

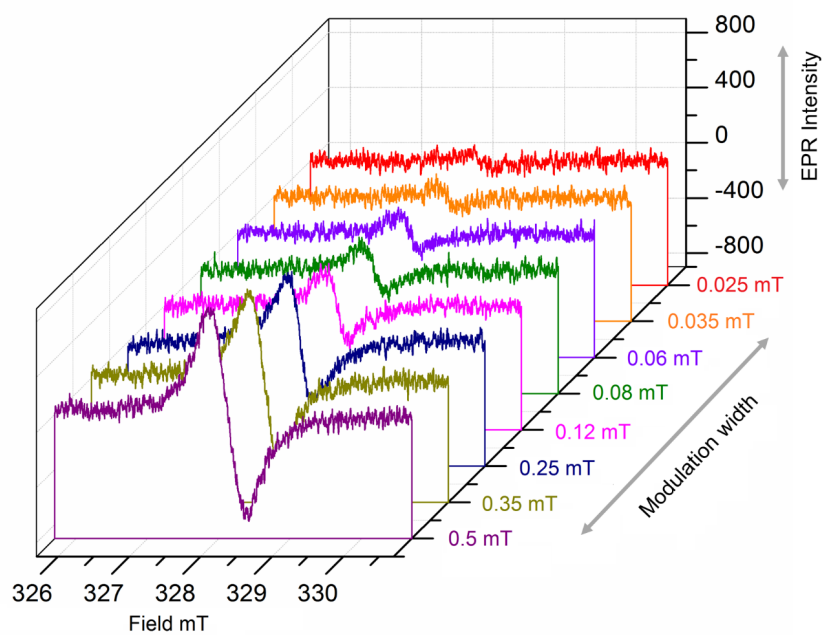


**Figure S18.** The dependence of the observed EPR resonance signal from the experimental modulation width used within signal acquisition for the G(OH)F system. The sample temperature was kept constant in all measurements ( $T = 213$  K). Parameters: 9.170957 GHz, 100 kHz modulation frequency, 0.1 mW microwave power, 2 min sweep time, 0.03 s time constant, and  $\pm 2.5$  mT sweep width.

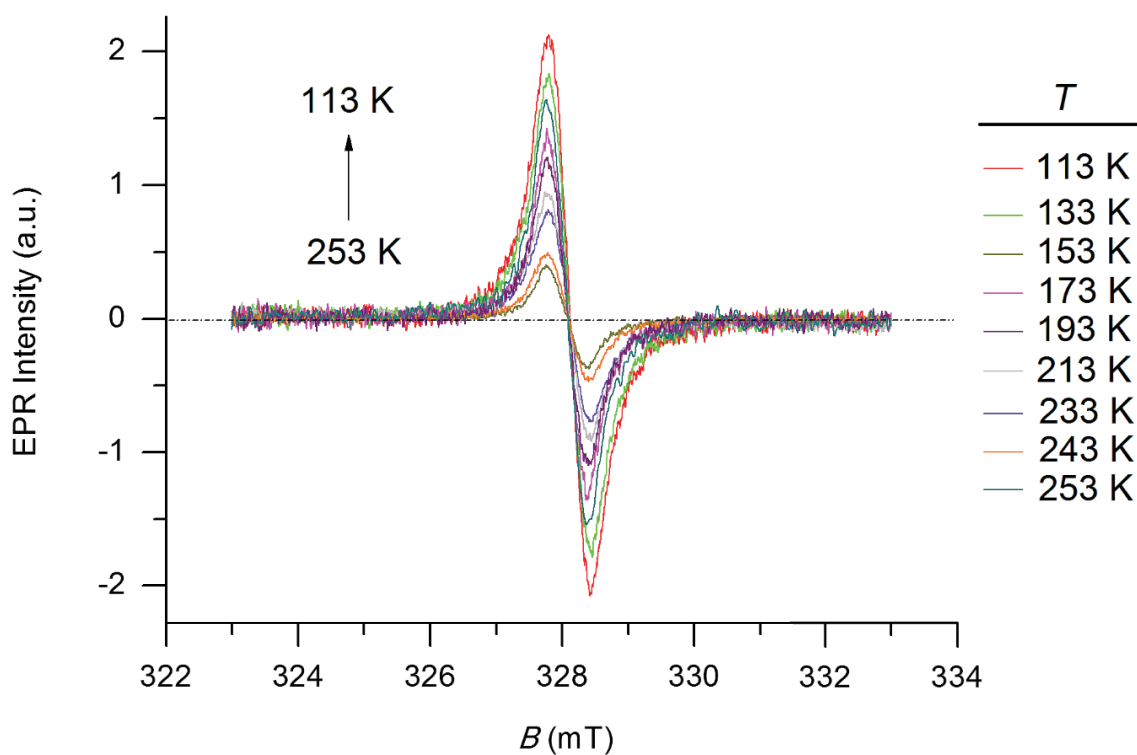


**Figure S19.** The temperature dependence of the observed EPR resonance signal for the G(OH)F system, showing an increase in the signal upon decreasing the temperature, from 253 K down to 113 K. Parameters: 9.17048 GHz, 100 kHz modulation frequency, 100  $\mu$ W microwave power, 2 min sweep time, 0.03 s time constant, and 0.35 mT modulation width.

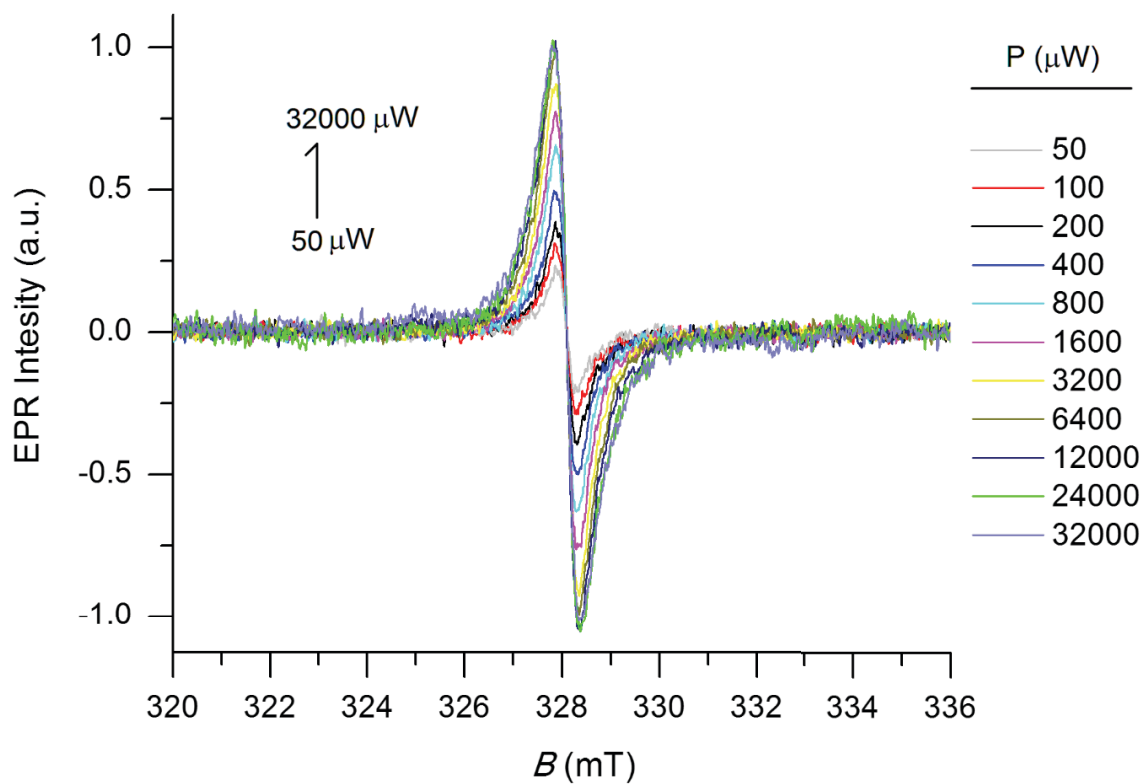


**Figure S20.** The X-band (9.17 GHz) EPR saturation spectra of the G(OH)F system, recorded in function of increasing microwave powers at  $T = 133$  K (from 0.05 mW to 32 mW).

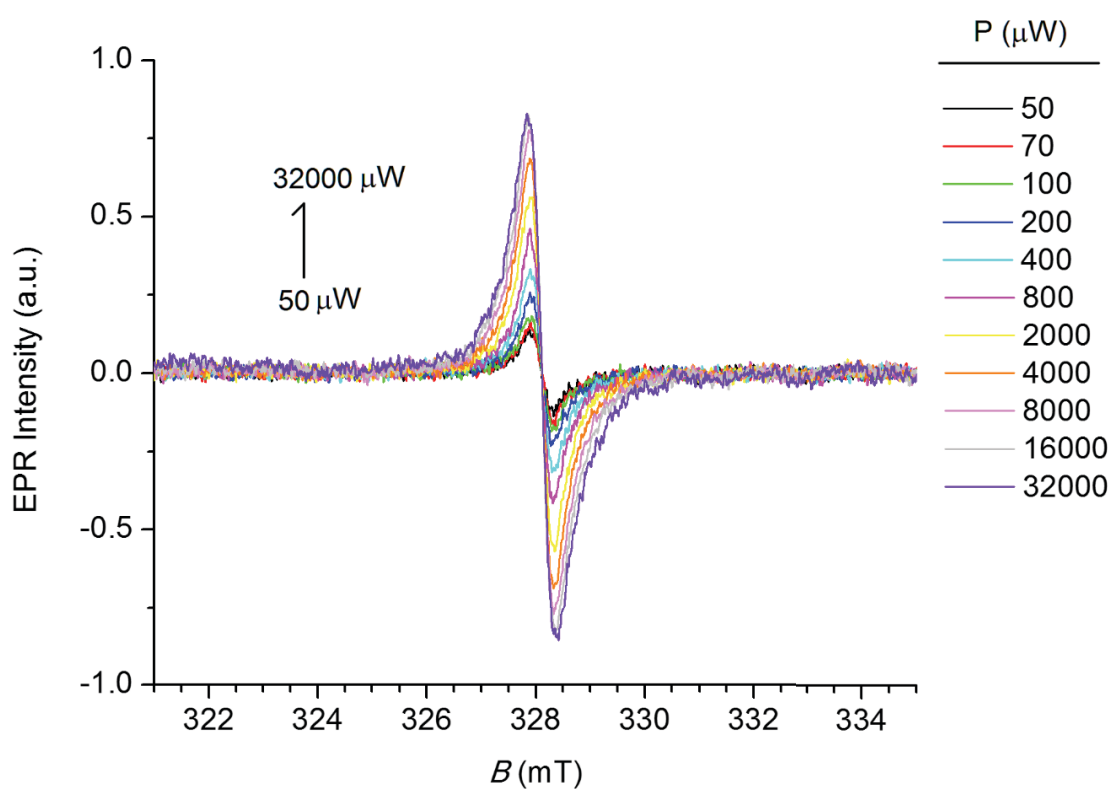


**Figure S21.** The X-band (9.17 GHz) EPR saturation spectra of the G(OH)F system, recorded in function of increasing microwave powers at  $T = 173$  K (from 0.05 mW to 32 mW).

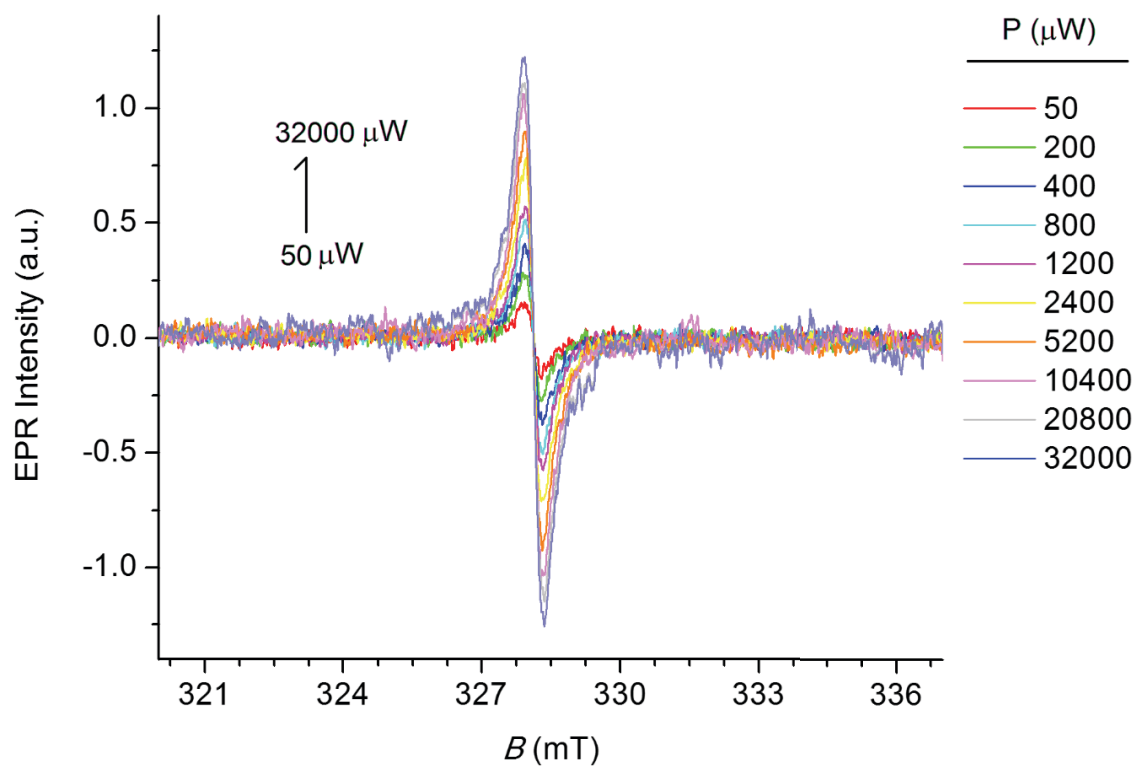


**Figure S22.** The X-band (9.17 GHz) EPR saturation spectra of the G(OH)F system, recorded in function of increasing microwave powers at  $T = 213$  K (from 0.05 mW to 32 mW).

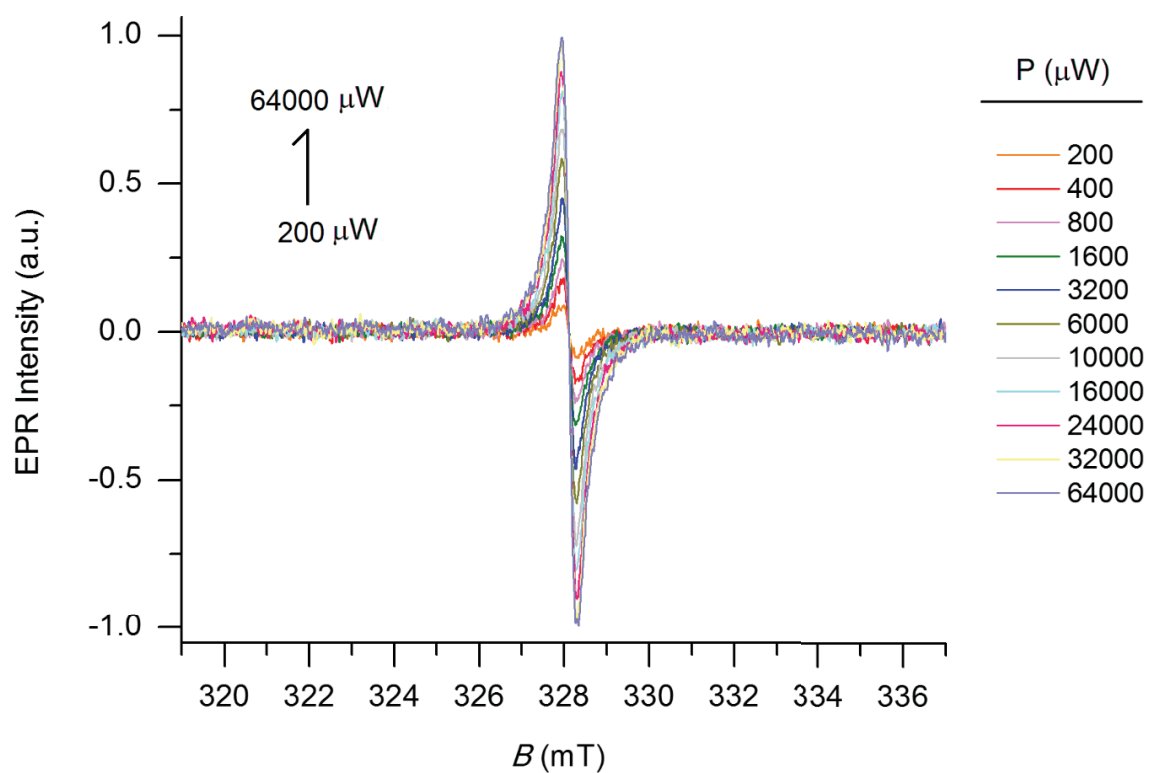


**Figure S23.** The X-band (9.17 GHz) EPR saturation spectra of the G(OH)F system, recorded in function of increasing microwave powers at  $T = 253$  K (from 0.200 mW to 64 mW).

## Calculations of G(OH)F Structures

To understand the structural, electronic, and magnetic features of the G(OH)F systems, we performed periodic density functional theory (DFT) calculations on models of  $C_{18}(OH)_x F_y$  ( $x = 3, 4$ ;  $y = 5, 6$ ) with a stoichiometry very close to the experimental one ( $x = 3.4$ ;  $y = 6$ ). We considered at least 100 randomly chosen structural arrangements for each stoichiometry to model the random nature of fluorographene derivatization, in which both reductive defluorination and substitution of F by OH take place simultaneously.<sup>S1-S3</sup>

During the synthesis, both reductive defluorination and substitution of  $-F$  by an  $-OH$  group take place simultaneously and are initiated at defect sites.<sup>S2</sup> Whereas the defluorination is largely driven by thermodynamics, the nucleophilic attack can depend on kinetic factors, site availability and local topology (see Figure S24 in the Supporting Information). Therefore, various structures can be formed. Since the migration of functional groups over the graphene surface is energetically prohibited because of instability of the final state and/or high activation energies (see Figure S25 in the Supporting Information), the created motifs remain stable. The final structural organization of G(OH)F systems was thus not only dictated by the thermodynamic stability of the individual structures but also the kinetics and random arrangement of defects over the surface of the starting fluorographene. We focused on identification of structural motifs that can imprint room temperature ferromagnetism into the G(OH)F system.

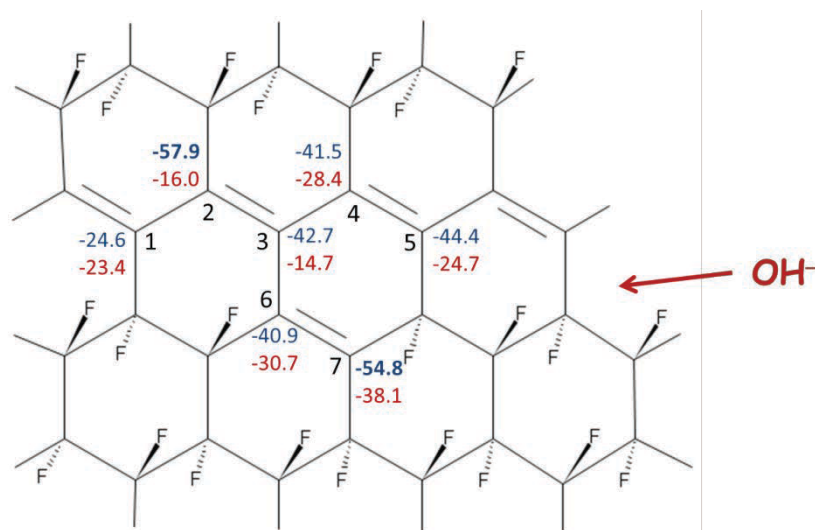


**Figure S24.** Reaction energies (in kcal/mol) for the nucleophilic attack of  $OH^-$  anion on partially fluorinated graphene ( $C_{18}F_{10}$ ) calculated at the  $\omega B97X-D/6-31+G(d)$  level of theory. Blue/red values correspond to the formation of singlet/triplet states.

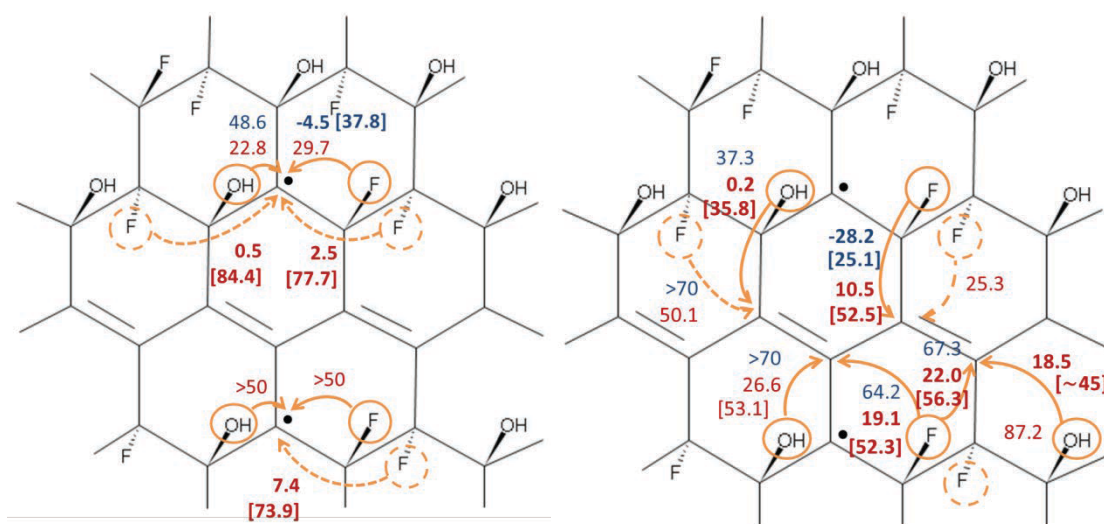


**Figure S25.** Kinetic stability of a typical ferromagnetic structure of  $C_{18}(OH)_4F_6$  assessed at the  $\omega$ B97X-D/6-31+G(d) level of theory. Blue/red values (in kcal/mol) correspond to the formation of singlet/triplet states by a migration of a fluorine atom or a hydroxyl group either to a neighboring radical carbon site (right) or to a carbon located on the conjugated chain (left). The barriers for possible channels are given in brackets.

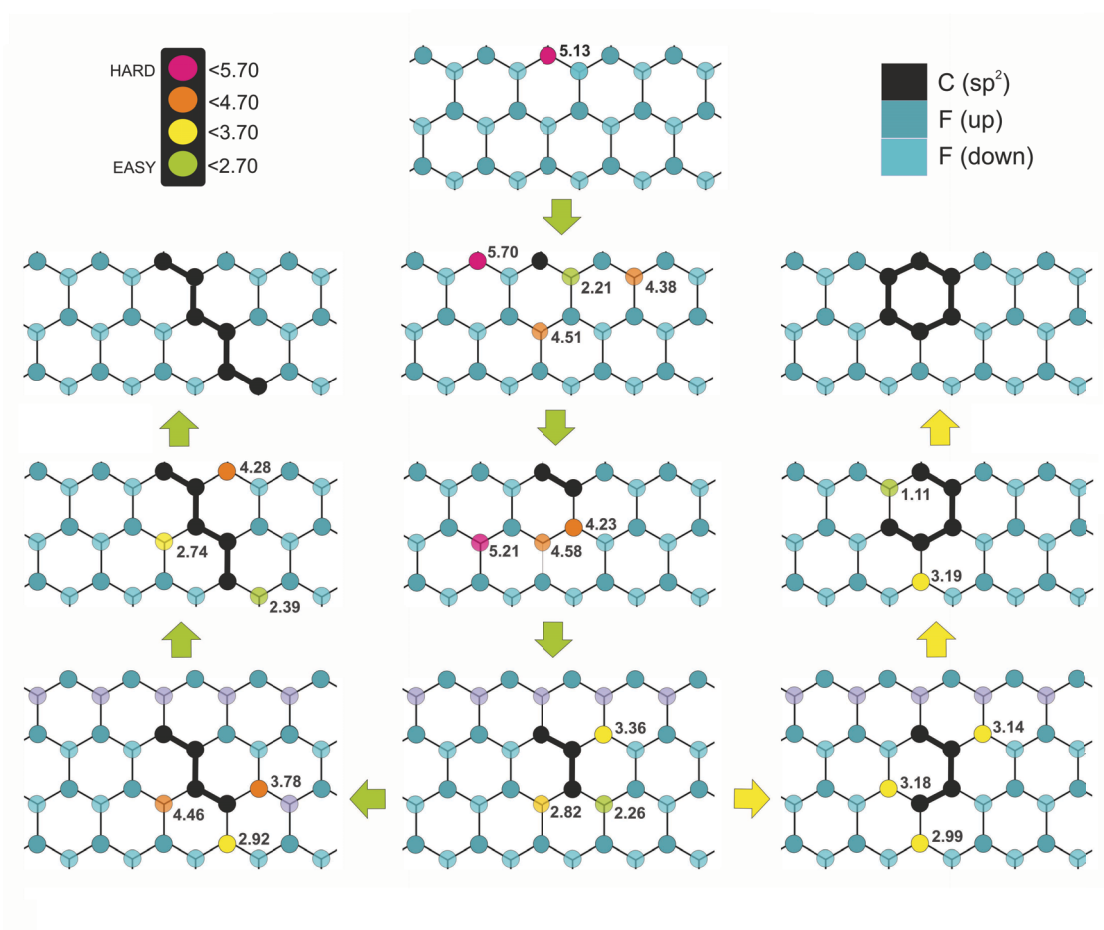


**Figure S26.** Bond dissociation energies (BDEs) of fluorine atoms of fluorographene indicating preferential defluorination pathways leading to the  $sp^2$  zigzag motif formation. BDEs (in eV, see color code) were calculated by DFT-PBC on  $C_{18}F_n$  ( $n = 18-12$ ).

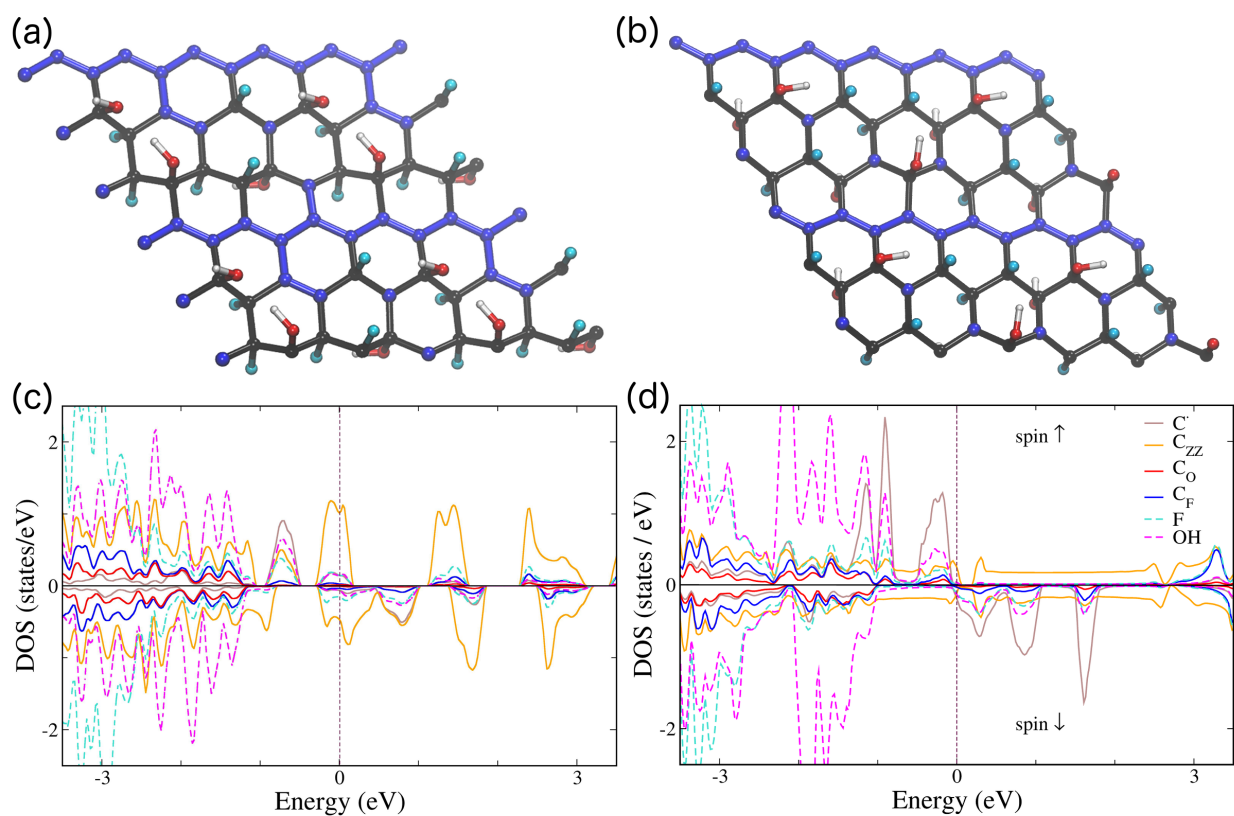


**Figure S27.** Theoretical calculations for the G(OH)F systems. (a, b) Prototypical G(OH)F structures with a stoichiometry of  $C_{18}(OH)_3F_5$  (see panel (a)) and  $C_{18}(OH)_4F_5$  (see panel (b)) typically consisting of  $sp^2$ -conjugated zigzag chains passing through an  $sp^3$  domain and radical centers (both motifs are highlighted in blue) both isolated in the  $sp^3$  domain and attached as a side part of the  $\pi$ -chain. (c, d) The corresponding atom resolved spin-polarized density of states (DOS) plots, cf. Figure 4 in the main text, which indicate on a synergistic interplay between the superexchange coupling the radicals to the  $sp^2$  zigzag chains and the  $\pi$ -electron system transferring the coupling between  $sp^3$  strips.

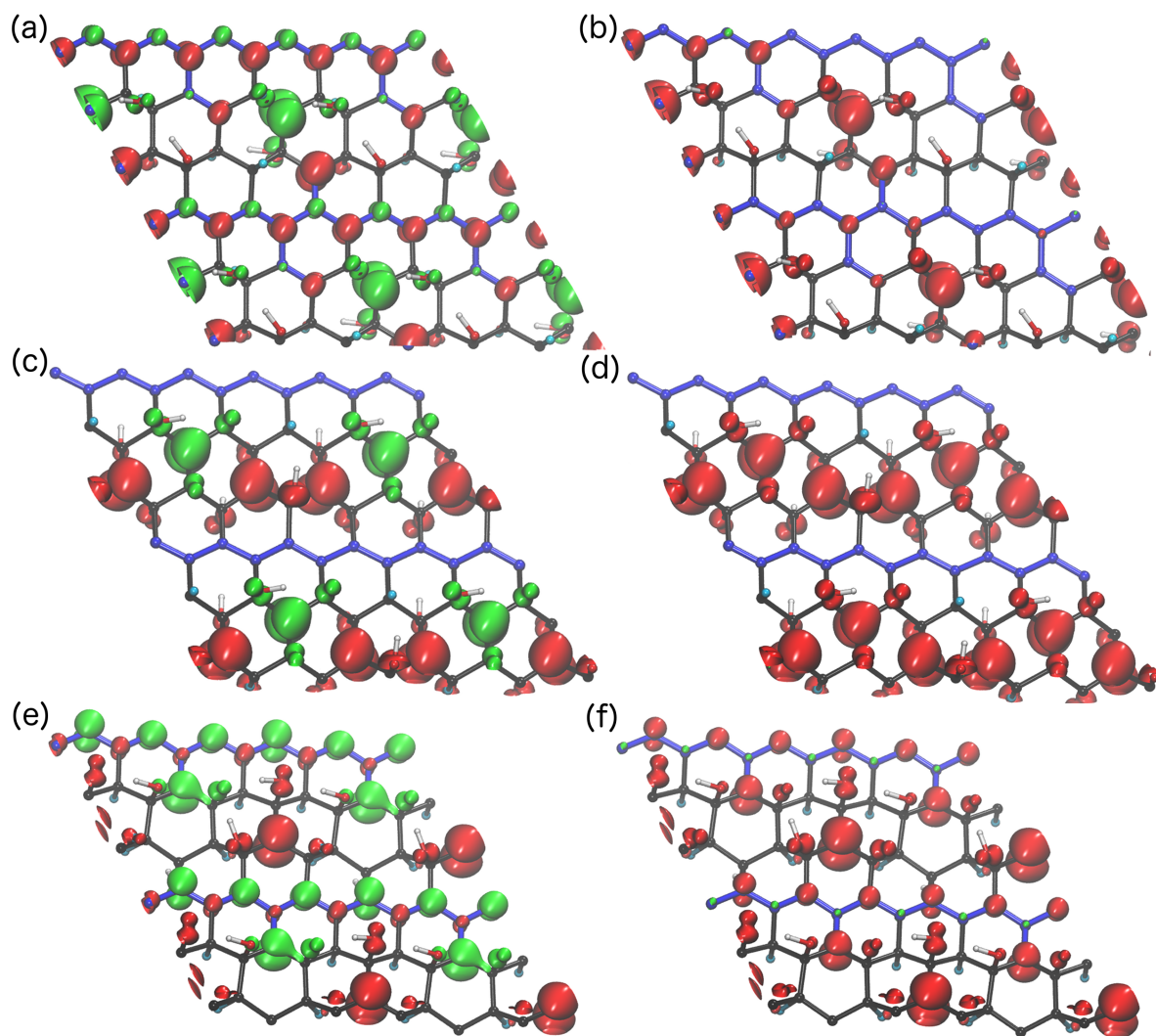


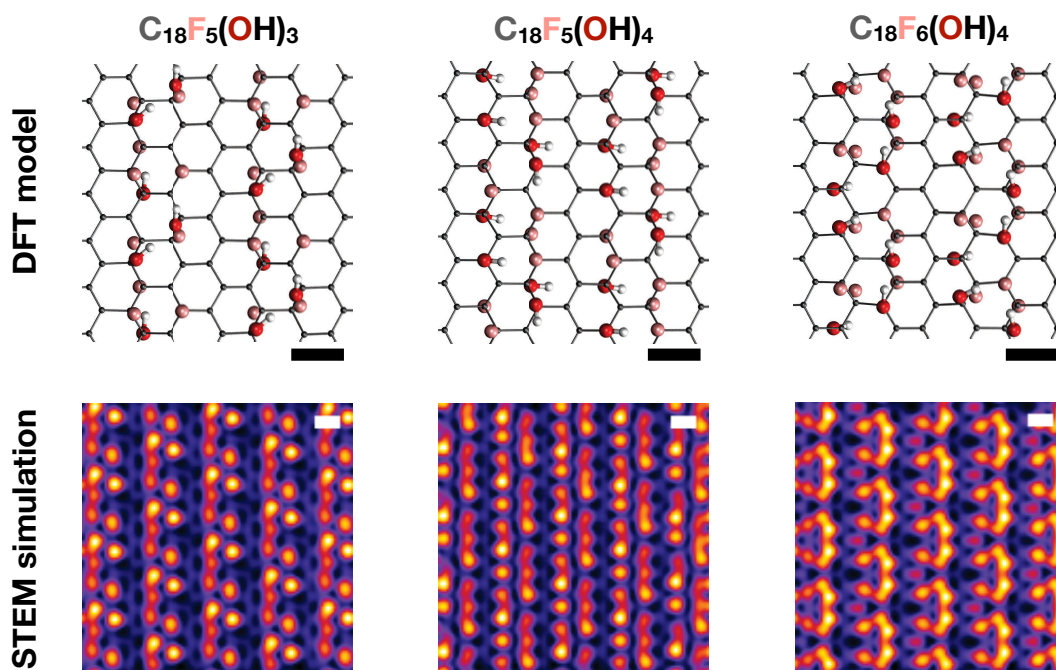
**Figure S28.** Theoretical calculations for the G(OH)F systems: (a, b)  $C_{18}(OH)_3F_5$ , (c, d)  $C_{18}(OH)_4F_5$ , and (e, f)  $C_{18}(OH)_4F_6$ . The calculations converged to ferromagnetic structures and the spin-flip led to solutions with non-zero total magnetic moments, *i.e.*, ferrimagnetic states with the spin-flip energy below 60 meV. The spin density distribution in ferrimagnetic and ferromagnetic G(OH)F structures are shown in panels (a), (c), (e) and panels (b), (d), (f), respectively. The red and green hypersurfaces show contours of positive and negative magnetization density, respectively.

## Scanning Transmission Electron Microscopy Measurements and Simulations

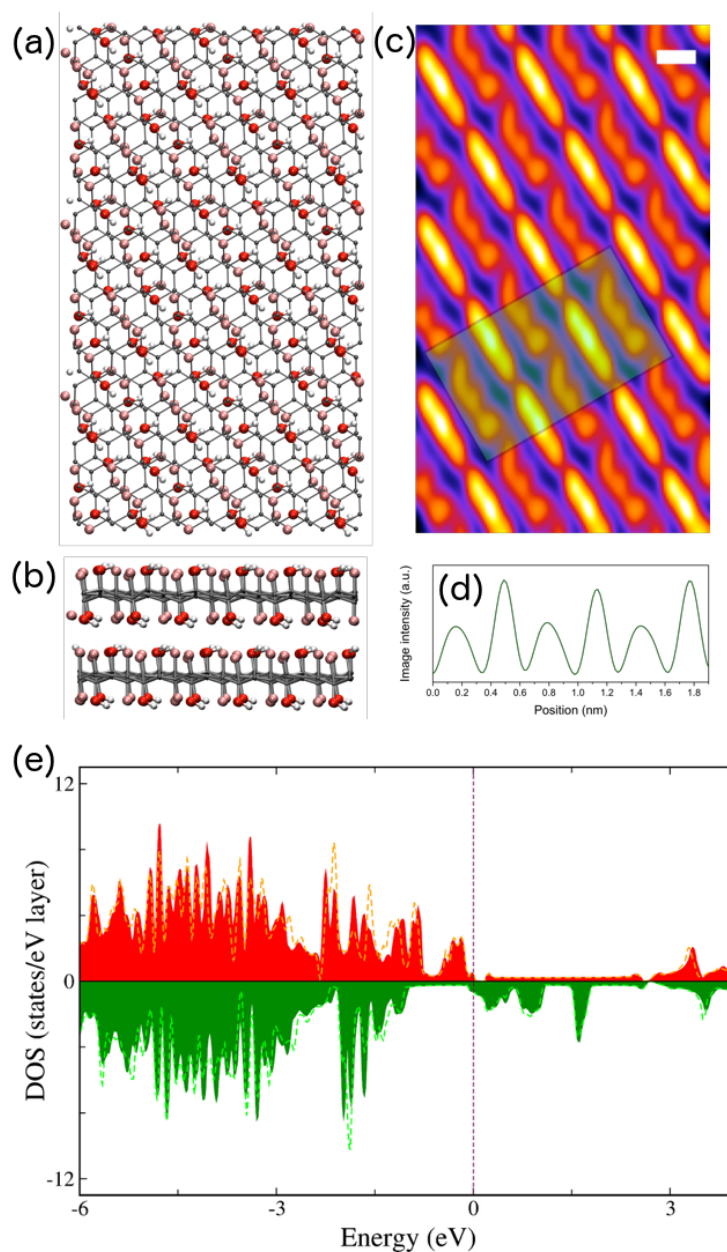
To obtain insights into the atomic structure of ferromagnetic G(OH)F systems, we used scanning transmission electron microscopy (STEM). Although covalently bound functional groups are not expected to be stable against electron irradiation,<sup>S4</sup> and the loss of  $sp^2$  hybridization can enhance otherwise negligible<sup>S5</sup> ionization damage, in multilayered structures, both effects may be mitigated. After dispersing the synthesized material on holey carbon support films, we detected aggregates that were at places thin enough to distinguish near-atomic contrast.

Figure 5a in the main text shows a typical example of one such aggregate. Closer inspection of a thin region (see Figure 5b in the main text) revealed repeating linear contrast visible in the thinner regions. An even closer view (see Figure 5c in the main text) allowed us to measure the periodicity of the contrast as  $\sim 0.29$  nm (line profile shown in Figure 5f in the main text). To ascertain the chemical identity of the imaged regions, we performed electron energy loss spectroscopy (EELS). Spectrum images recorded over a transition between a thinner and thicker region (see Figure 5d,e in the main text) clearly demonstrated the presence of oxygen in the sample. The high-resolution EELS spectrum shown in Figure 5g in the main text is characteristic of  $-OH$  groups.<sup>S6</sup>

To understand the source of the repeating linear contrast, we created several candidate structures and simulated their STEM/MAADF images (MAADF stands for medium-angle annular dark-field imaging option). The contrast of monolayer structures did not directly match the experimental images (see Figure S29 in the Supporting Information), although the two lines of functional groups in  $C_{18}F_5(OH)_4$  had the correct separation. However, these lines overlapped in a projected view of a relaxed bilayer of this structure (see Figure S30a,b in the Supporting Information), with apparent separation very close to our experimental images. The image simulation shown in Figure S30c in the Supporting Information has the correct single periodicity, although as seen from the line profile plotted in Figure S30d in the Supporting Information, the intensities of the peaks alternate. Likely our experimental image corresponds to multiple layers, averaging out this alternation.



**Figure S29.** Comparison on simulated STEM/MAADF images (bottom, colored with ImageJ lookup table “Fire” to enhance contrast) for the three candidate monolayer structures relaxed by DFT (top, C atoms shown in grey, O red, F pink, and H white). The scale bars in both cases are 0.29 nm.



**Figure S30.** Identification of repeating linear features. (a) Top view of the candidate DFT model supercell of  $C_{18}F_5(OH)_4$  bilayer relaxed using an empirical vdW correction (C atoms shown in grey, O red, F pink, and H white). (b) Side view. (c) Quantitative STEM image simulation of the structure, with a Gaussian blur of a radius of  $0.5 \text{ \AA}$  applied, and colored with the ImageJ lookup table “Fire”. (d) Line profile of the area overlaid in green in panel (c), indicating a repeating intensity variation with a period of  $0.32 \text{ nm}$ . (e) Spin and layer-resolved DOS of the  $C_{18}(OH)_4F_5$  bilayer. DOS’s of different layers are discriminated by solid/broken lines.

## Supporting Table

**Table S1.** Content of various selected metals in the synthesized G(OH)F sample, determined from the inductively coupled plasma mass spectrometry (ICP-MS) technique.

Ti (ppm)	Cr (ppm)	Fe (ppm)	Co (ppm)	Ni (ppm)	Cu (ppm)	Zn (ppm)
0.3	<0.1	14.9	0.2	8.9	<0.1	20.3

## References for Supporting Information File

(S1) Dubecký, M.; Otyepková, E.; Lazar, P.; Karlický, F.; Petr, M.; Čépe, K.; Banáš, P.; Zbořil, R.; Otyepka, M. Reactivity of Fluorographene: A Facile Way toward Graphene Derivatives. *J. Phys. Chem. Lett.* **2015**, *6*, 1430–1434.

(S2) Medved', M.; Zoppellaro, G.; Ugolotti, J.; Matochová, D.; Lazar, P.; Pospíšil, T.; Bakandritsos, A.; Tuček, J.; Zbořil, R.; Otyepka, M. Reactivity of Fluorographene is Triggered by Point Defects: Beyond the Perfect 2D World. *Nanoscale* **2018**, *10*, 4696–4707.

(S3) Matochová, D.; Medved', M.; Bakandritsos, A.; Steklý, T.; Zbořil, R.; Otyepka, M. 2D Chemistry: Chemical Control of Graphene Derivatization. *Phys. Chem. Lett.* **2018**, *9*, 3580–3585.

(S4) Tararan, A.; Zobelli, A.; Benito, A. M.; Maser, W. K.; Stephan, O. Revisiting Graphene Oxide Chemistry *via* Spatially-Resolved Electron Energy Loss Spectroscopy. *Chem. Mater.* **2016**, *28*, 3741–3748.

(S5) Susi, T.; Hofer, C.; Argentero, G.; Leuthner, G. T.; Pennycook, T. J.; Mangler, C.; Meyer, J. C.; Kotakoski, J. Isotope Analysis in the Transmission Electron Microscope. *Nat. Commun.* **2016**, *7*, 13040.

(S6) Garvie, L. A. J. Can Electron Energy-Loss Spectroscopy (EELS) Be Used to Quantify Hydrogen in Minerals from the O K Edge? *Am. Mineral.* **2010**, *95*, 92–97.